

UNIVERSITY OF CALIFORNIA

Los Angeles

Design and Applications of
Resonant Electro-Optic Time Lenses

A thesis submitted in partial satisfaction of the
requirements for the degree Master of Science
in Electrical Engineering

by

Ryan Patrick Scott

1995

© Copyright by
Ryan Patrick Scott
1995

The thesis of Ryan Patrick Scott is approved.

Oscar M. Stafsudd

Ming C. Wu

Brian H. Kolner, Committee Chair

University of California, Los Angeles

1995

TABLE OF CONTENTS

List of Figures	v
Acknowledgements	vii
Abstract	viii
Chapter 1. Introduction	1
1.1 Space-Time Analogy	2
General Wave Equation	3
Paraxial Wave Equation	4
Dispersive Wave Equation	6
Diffusion Equation	8
Quadratic Phase Modulation	10
1.2 Electro-Optic Phase Modulation	12
Focal Time	15
<i>f</i> -number and Resolution	17
Chapter 2. Electro-Optic Time Lenses	21
2.1 Design Considerations	22
RF Design	22
Velocity Matching	23
Resonator Design	25
Mechanical Considerations	28
Thermal Considerations	30
2.2 Construction	31
2.3 Modulator Characterization	32
2.4 Future Investigation	34

Chapter 3. Active Pulse Compression	36
3.1 Self-Phase Modulation and Optical Pulse Compression	36
3.2 Electro-Optic Pulse Compression	39
Amplitude Noise	40
Timing Jitter	40
“Single Knob” Adjustable Pulse Compression	42
3.3 Design of a Multiple-Pass Optical Cavity	45
Timing Requirements	46
Ray Path Analysis	48
Beam Geometry	50
Focusing Properties	52
3.4 Experimental Results of an Active Pulse Compressor	54
3.5 Future Investigation	58
Chapter 4. Active Additive Pulse Modelocking	60
4.1 Additive Pulse Modelocking	61
4.2 Active Nonlinear Element	63
Experimental Configuration	63
External Cavity Stabilization	65
4.3 Some Experimental Results	67
4.4 Future Investigation	72
Chapter 5. Conclusion	73
Appendix A	75
References	80

LIST OF FIGURES

1. Wave Equation Approximations	2
2. Temporal and Spatial Imaging.....	10
3. Thin Lens.....	11
4. Copropagating Electric and Optical Fields	13
5. Temporal Imaging Configuration	18
6. Rectangular Resonator	26
7. Ridge-Waveguide Resonator	27
8. BeCu Spring Holding Crystal.....	29
9. Resonant Frequency vs. Temperature Plot	33
10. Self-Phase Modulation	38
11. BeCu Spring Holding Crystal.....	39
12. Spatial Beam Jitter	41
13. Active Compressor Schematic	43
14. Pulse Shape vs. RF Power	44
15. Compression Ratio	45
16. Cavity Timing Schematic.....	47
17. 1-Dimensional Optical Cavity	49
18. 2-Dimensional Optical Cavity	51
19. Beam Clipping Restriction Detail.....	53
20. Experimental Multiple-Pass Cavity	55

21. Autocorrelation of Compressed Pulse	57
22. Spectrum of Compressed Pulse	58
23. Compression with a Compound Time Lens	59
24. Additive Pulse Modelocking Configuration	62
25. Active APM Configuration	64
26. External Cavity Peak Power	66
27. AAPM Intensity Noise	67
28. AAPM Autocorrelation Trace	68
29. AAPM Pulse from Photodetector	68
30. AAPM Characteristics vs. RF Power	69
31. Autocorrelation of Astable Mode	70
32. Spectrum of AAPM Pulse	71
33. Pulse and Time Lens	75
34. Pulse and Dispersion	76

ACKNOWLEDGEMENTS

First, I want to thank my advisor and mentor, Professor Brian Kolner, for his encouragement, vigor, and determination to always do what is best for the student. I am greatly indebted to Professor Neville Luhmann and the Airforce's Advanced Thermionics Research Initiative for supporting much of the work in this thesis and for allowing me to use a workstation and HFSS.

For their abundant contributions and friendship, I am thankful to fellow graduate students Corey Bennett and Bill Stanton. Corey's work during the early stages of active pulse compression, and especially his work on the multiple pass optical cavity were indispensable. Also, the research performed by Bill on different waveguide structures was particularly helpful. I would like to extend my appreciation to Judy Karin for her careful reading of this thesis.

Most of all, I wish to thank my parents, family, and close friends. Their concern, encouragement, and advice will always be remembered and welcome.

Ryan Scott
Los Angeles, California
May 1995

ABSTRACT OF THE THESIS

Design and Applications of Resonant Electro-Optic Time Lenses

by

Ryan Patrick Scott

Master of Science in Electrical Engineering

University of California, Los Angeles, 1995

Professor Brian H. Kolner, Chair

The differential equations governing diffraction of fields in space and dispersion of pulses in dielectrics are nearly identical. The resemblance of these two processes has led to a well known theory in which the manipulation of optical waveforms in time is analogous to spatial imaging. From this theory, a *time lens* is a device or process which is capable of imparting quadratic phase in time to an optical waveform.

This thesis investigates in detail the design of a time lens based on a resonant cavity electro-optic modulator. Consideration is given to the RF, mechanical, and thermal aspects of the design, including the fundamental issues underlying maximization of the modulation efficiency. Also, experimental results of a working time lens are presented.

Application of this time lens to an active optical pulse compression system is studied. An explication of the design of a multiple-pass optical cavity to enhance the modulation efficiency of the time lens is given. Additionally, ways in which this

system can be used to eliminate pulse timing jitter and stabilize amplitude noise are discussed. To demonstrate the system, 85 ps pulses were compressed to less than 6 ps, a compression ratio of 14:1.

Finally, a new technique for shortening modelocked laser pulses is described. This method incorporates a time lens as an active element in an external cavity and is designated *active additive pulse modelocking*. With this technique, the average power of the laser is maintained while the pulse width is shortened by a factor of four.

Within science many ideas are conveyed using analogies to well known phenomena. For example, in quantum mechanics the propagation of photons can be analogous to the movement of either particles or waves depending on the particular event being described, even though a photon is neither a particle nor a wave. In many areas of science, from physics to chemistry, the motion of a simple harmonic oscillator is used to describe a variety of different events including the motion of an electron bound to an atom. These analogies have led to a better understanding of the phenomena which they describe. Many years ago, the analogy between the spatial diffraction of beams and the temporal dispersion of pulses was presented by several authors [1–3]. In fact, as I will explain in the following section, mathematically, the two processes are practically identical. This has led to exciting new ideas in the treatment of light propagating in time. For example, in the spatial treatment of light we have lenses which can be used to form imaging systems. Imagine, in the temporal case, *time lenses* which can be used to form temporal imaging systems, allowing us to directly change the time scale on which optical events take place! From the simple compression of optical pulses to the expansion of ultrafast optical waveforms emanating from chemical reactions, the potential applications of such a system are remarkable.

1.1 Space-Time Analogy

An elegant analogy exists between the mathematical description of the paraxial diffraction of optical beams confined in space and the temporal dispersion of optical pulses in dielectrics [4–6]. It is possible to see from this analogy that temporal quadratic phase modulation in time is equivalent to a thin lens in space. Thus, if this “time lens” (quadratic phase modulation) were used with the proper amount of dispersion, a temporal imaging system could be fabricated. Most of the properties associated with a spatial imaging system would apply to the temporal system. Concepts such as focal length, f -number, magnification, and resolution all have temporal analogs and these are investigated further in the following sections.

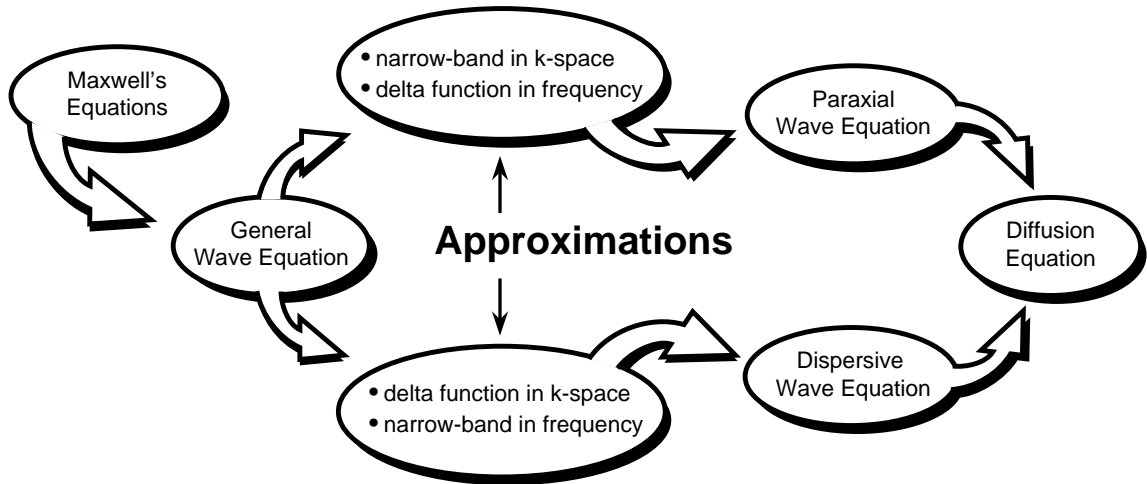


Figure 1. Schematic derivation of dispersive and diffractive (paraxial) wave equations from Maxwell’s equations. Approximations are made to the general wave equation which determine whether the resulting wave equation describes the spatial or temporal nature of the propagation. These wave equations are of the same form as the simple diffusion equation.

In order to understand how the analogy may be arrived at mathematically, I have broken down the process to a schematic illustration similar to the one used by Kolner (Fig. 1) [6]. From Maxwell’s equations we can derive the “general” wave

equation which describes the space-time evolution of an arbitrary electromagnetic field distribution. To find an exact solution to the equation, some approximations which limit our interest to either the spatial or temporal evolution of the EM field are made. In the spatial case, the approximations consist of assuming that the energy is confined to a narrow region of space along the path of propagation (paraxial) and that this energy is monochromatic. The paraxial wave equation then follows from these approximations. When treating the temporal case, we consider the fields to be propagating in only one direction (infinite plane wave), and assume that the frequency spectrum is confined to a narrow-band around the carrier. This yields the narrow-band dispersive wave equation. Now, both the paraxial and dispersive wave equation are complex forms of the heat diffusion equation. Therefore, we can expect the behavior of propagating electromagnetic fields to have some similarities to heat diffusion.

General Wave Equation

In terms of free charges and currents, Maxwell's equations read [7]

$$\begin{aligned}
 \text{(i)} \quad \vec{\nabla} \times \vec{E} &= -\frac{\partial \vec{B}}{\partial t} & \text{(iii)} \quad \vec{\nabla} \cdot \vec{D} &= \rho_f \\
 \text{(ii)} \quad \vec{\nabla} \times \vec{H} &= \vec{J}_f + \frac{\partial \vec{D}}{\partial t} & \text{(iv)} \quad \vec{\nabla} \cdot \vec{B} &= 0.
 \end{aligned} \tag{1}$$

The constitutive relations are given below for electromagnetic fields in a lossless (conductivity $\sigma = 0$), nonresonant, isotropic dielectric medium with a dielectric constant ϵ or, equivalently, an electric susceptibility χ .

$$\vec{B} = \mu_0 \vec{H} \quad \vec{J} = \sigma \vec{E} = 0 \quad \vec{D} = \epsilon \vec{E} = \epsilon_0 [1 + \chi] \vec{E}. \tag{2}$$

If we assume that the medium has no free charge ($\vec{\nabla} \cdot \vec{D} = 0$) and apply the curl

operator to Faraday's Law (i) of Eq. (1) we get,

$$\vec{\nabla} \times (\vec{\nabla} \times \vec{E}) = \vec{\nabla} (\vec{\nabla} \cdot \vec{E}) - \vec{\nabla}^2 \vec{E} = \vec{\nabla} \times \left(-\frac{\partial \vec{B}}{\partial t} \right) \quad (3)$$

$$= -\frac{\partial}{\partial t} (\vec{\nabla} \times \vec{B}) = -\mu_0 \frac{\partial^2}{\partial t^2} (\epsilon_0 \vec{E} + \vec{P}), \quad (4)$$

where the linear, and possibly dispersive, polarization of the medium is given by $\vec{P} = \epsilon_0 \chi \vec{E}$. Finally, by applying a little more algebra we obtain

$$\vec{\nabla}^2 \vec{E} - \mu_0 \epsilon_0 \frac{\partial^2 \vec{E}}{\partial t^2} = \mu_0 \frac{\partial^2 \vec{P}}{\partial t^2}. \quad (5)$$

This is the 'general' wave equation. An analogous expression for the magnetic field can be similarly derived from (ii) and (iv) of Eq. (1).

Paraxial Wave Equation

Assuming a sinusoidal electromagnetic field oscillating in free space ($x=0$) at angular frequency ω_0 , Fourier transformation of Eq. (5) yields

$$\vec{\nabla}^2 \vec{E} - \omega_0^2 \mu_0 \epsilon_0 \vec{E} = 0, \quad (6)$$

or

$$\left(\vec{\nabla}^2 + k^2 \right) \vec{E} = 0, \quad (7)$$

where the propagation constant

$$k = \omega_0 \sqrt{\mu_0 \epsilon_0} = \frac{2\pi}{\lambda}. \quad (8)$$

Suppose we now write a vector component (z -axis propagation) of the complex electric field \vec{E} in the form

$$\mathbf{E}(x, y, z) \equiv E(x, y, z) e^{-ikz}, \quad (9)$$

where we have factored out the rapid phase variation in the z -direction. This is appropriate for a wave propagating primarily in the $+z$ direction. The function $E(x, y, z)$ is an envelope that changes slowly in the transverse direction as the wave propagates. Entering the form of Eq. (9) into the wave equation (5) produces the reduced wave equation

$$\frac{\partial^2 E}{\partial x^2} + \frac{\partial^2 E}{\partial y^2} + \frac{\partial^2 E}{\partial z^2} - 2ik \frac{\partial E}{\partial z} = 0. \quad (10)$$

Since we are only concerned with light confined near the axis of propagation, z , the effects of diffraction on the beam profile $E(x, y, z)$ will be small. In other words, the phase variation perpendicular to z is much less than the phase variation of one complete cycle in phase that occurs in one wavelength due to the phase term in (9). Therefore, we can make the *paraxial approximation*

$$\left| \frac{\partial^2 E}{\partial z^2} \right| \ll \left| \frac{\partial^2 E}{\partial x^2} \right|, \quad \left| \frac{\partial^2 E}{\partial y^2} \right|, \quad \left| 2k \frac{\partial E}{\partial z} \right|. \quad (11)$$

With this approximation we can drop the $\partial^2 E / \partial z^2$ term in (10), and thus we have the so-called ‘paraxial wave equation’

$$\nabla_T^2 E - 2ik \frac{\partial E}{\partial z} = 0 \quad (12)$$

where the Laplacian operator in transverse coordinates is

$$\nabla_T^2 \equiv \frac{\partial^2}{\partial x^2} + \frac{\partial^2}{\partial y^2}. \quad (13)$$

This may also be written in a form more appropriate for later comparison,

$$E_z = -\frac{i}{2k} (E_{xx} + E_{yy}), \quad (14)$$

where the subscripts on the amplitude profiles indicate partial differentiation with respect to the coordinate.

Note that the paraxial wave equation controls the evolution of the electric field envelope $E(x, y, z)$ as it propagates along the z -axis. In the formalism of partial differential equations, (14) is a parabolic equation. It can be described as having a generalized complex diffusion term, $-i/2k$, for the field envelope in the transverse coordinate. This imaginary diffusion term causes the field envelope to broaden as it propagates, similar to the way a temperature distribution will spread with time, but for a different reason. In the following section, we will see that the dispersive phenomena of optical pulses is governed by a similar equation.

Dispersive Wave Equation

If we assume no transverse variation in the electric field (i.e., an infinite plane wave) then $\vec{\nabla} \rightarrow \partial/\partial z$ and Eq. (5) becomes

$$\frac{\partial^2 E(z, t)}{\partial z^2} - \mu_0 \epsilon_0 \frac{\partial^2 E(z, t)}{\partial t^2} = \mu_0 \frac{\partial^2 P(z, t)}{\partial t^2}, \quad (15)$$

with

$$E(z, t) \equiv \text{Re } A(z, t) e^{i[\omega_0 t - \beta(\omega_0)z]}. \quad (16)$$

In this case ω_0 is again the midband or carrier frequency, $A(z, t)$ is the complex amplitude envelope function, and $\beta(\omega_0)$ is the dispersive propagation constant at the midband frequency. Now, we wish to form a differential equation that describes the evolution of $A(z, t)$. Siegman [8] has shown that this can be done by writing the polarization term on the right side of Eq. (15) as product of two quantities. The first is an integration over frequency space of the frequency dependent susceptibilities and the other is the Fourier transform of the electric field $E(z, t)$. This can be

shown by using the following relations,

$$P(z, t) = \frac{1}{2\pi} \int_{-\infty}^{+\infty} \mathcal{P}(z, \omega) e^{i\omega t} d\omega, \quad (17)$$

$$\mathcal{P}(z, \omega) = \epsilon_0 \chi(\omega) \mathcal{E}(z, \omega), \quad (18)$$

$$\begin{aligned} \mathcal{E}(z, \omega) &= \int_{-\infty}^{+\infty} E(z, t) e^{-i\omega t} dt \\ &= \int_{-\infty}^{+\infty} A(z, t) e^{-i\beta(\omega_0)z} e^{i(\omega_0 - \omega)t} dt, \end{aligned} \quad (19)$$

and a handful of Fourier transform theorems, we can write

$$\frac{\partial^2 P(z, t)}{\partial t^2} = -\frac{\epsilon_0}{2\pi} \int_{-\infty}^{+\infty} \omega^2 \chi(\omega) e^{i\omega t} d\omega \int_{-\infty}^{+\infty} A(z, t') e^{i[\omega_0 t' - \beta(\omega_0)z]} dt'. \quad (20)$$

Now, the quantity $\omega^2 \chi(\omega)$ is expanded about its midband value in the form

$$\begin{aligned} \omega^2 \chi(\omega) &\approx \omega_0^2 \chi(\omega_0) + \frac{d}{d\omega} [\omega^2 \chi(\omega)] \times (\omega - \omega_0) \\ &\quad + \frac{1}{2} \frac{d^2}{d\omega^2} [\omega^2 \chi(\omega)] \times (\omega - \omega_0)^2 + \dots \end{aligned} \quad (21)$$

with each of the derivatives evaluated at $\omega = \omega_0$. This is the same approximation which is commonly used to expand the propagation constant, $\beta(\omega)$. The polarization integral of Eq. (20) can now be evaluated using various integral identities as well as the following definitions:

$$\begin{aligned} \beta^2(\omega) &\equiv \mu_0 \epsilon_0 \omega^2 + \mu_0 \epsilon_0 \omega^2 \chi(\omega) \\ 2\beta \frac{d\beta}{d\omega} &\equiv 2\mu_0 \epsilon_0 \omega + \mu_0 \epsilon_0 \frac{d}{d\omega} [\omega^2 \chi(\omega)] \\ \left(\frac{d\beta}{d\omega} \right)^2 + \beta \frac{d^2 \beta}{d\omega^2} &\equiv \mu_0 \epsilon_0 + \frac{\mu_0 \epsilon_0}{2} \frac{d^2}{d\omega^2} [\omega^2 \chi(\omega)], \end{aligned} \quad (22)$$

where the midband group velocity is defined as $v_g(\omega_0) \equiv (d\beta/d\omega|_{\omega=\omega_0})^{-1}$ and the group velocity dispersion is given by $d^2\beta/d\omega^2|_{\omega=\omega_0}$. Take the approximations and

identities from above and substitute all of them into the wave equation (15). Apply a considerable amount of algebra, use the slowly varying envelope approximation to drop the second order derivatives in z , and Eq. (15) then reduces to the desired equation for the evolution of $A(z, t)$,

$$\left[\frac{\partial}{\partial z} + \frac{1}{v_g} \frac{\partial}{\partial t} - \frac{i}{2} \frac{d^2 \beta}{d\omega^2} \frac{\partial^2}{\partial t^2} \right] A(z, t) = 0. \quad (23)$$

An alternative form of the dispersive wave equation may be obtained by introducing a change of variables. Consider a traveling-wave coordinate system moving at the wave's group velocity [6],

$$\begin{aligned} \tau &= (t - t_0) - \left(\frac{z - z_0}{v_g} \right) \\ \xi &= z - z_0, \end{aligned} \quad (24)$$

where t_0 and z_0 are initial references. With these, Eq. (23) acquires a simpler form

$$\frac{\partial A(\xi, \tau)}{\partial \xi} = \frac{i}{2} \frac{d^2 \beta}{d\omega^2} \frac{\partial^2 A(\xi, \tau)}{\partial \tau^2}, \quad (25)$$

or, writing the derivatives as subscripts,

$$A_\xi = \frac{i}{2} \frac{d^2 \beta}{d\omega^2} A_{\tau\tau}. \quad (26)$$

This form should look familiar, especially when compared to the paraxial wave equation (14). Note that this form of the dispersive wave equation gives the pulse evolution centered on the envelope ($\tau = 0$) and traveling at the group velocity, v_g , using the parameter ξ as the propagation distance.

Diffusion Equation

If we look at Eq's. (14) and (26), their close resemblance to the heat equation becomes apparent. It is the similarity between these equations which allows for the

analogy. However, the differences are responsible for some of the most interesting properties of these wave equations. The simplest form of the one-dimensional heat equation in a source-free region can be written

$$T_t = cT_{xx}, \quad (27)$$

where the constant, c , is the diffusion term and is known as the *diffusivity* of the material. For a given material, this constant is

$$c = \frac{\kappa}{C\rho}, \quad (28)$$

where κ is the thermal conductivity, C is the specific heat, and ρ is the density. A nice physical interpretation of this can be described in the following way. If $T(\vec{r}, t)$ represents the temperature distribution, or curvature, in space and time within the medium, then the time rate of change of $T(\vec{r}, t)$ at a point \vec{r} is proportional to the product of the diffusivity and the local spatial curvature of the temperature distribution. Therefore, the steeper the curvature of the temperature field the faster the rate of temperature change at that point. This leads to the *diffusion* of the temperature field into neighboring regions of the medium.

Diffraction of fields in space have the same basic behavior. The more tightly a beam is confined in space, the greater the diffraction. This also holds true in the case of dispersion. The shorter the pulse envelope (greater local curvature), the faster it spreads out in time. Both of these phenomena are controlled by their corresponding “complex diffusivity” terms, which are present in the diffraction equation (14) and the dispersion equation (26). Owing to the imaginary nature of the diffusivity term, diffraction and dispersion are rather different from heat diffusion [6]. The imaginary

term causes a phase filtering of the Fourier spectra, thereby leading to broadening of the field envelope in real space. In heat diffusion, however, the temperature distribution broadening is caused by attenuation of the higher frequency Fourier components resulting from the presence of a real diffusivity coefficient.

Quadratic Phase Modulation

We have seen the analogy between dispersion and diffraction. Let us take advantage of this and present the idea of a temporal imaging system. In classical optics we form imaging systems using a lens and the proper amount of diffraction, via propagation in space, before and after the lens (Fig. 2a). If the analogy truly holds, then we should be able to form a “temporal imaging system” using the proper amount of dispersion before and after a “time lens” (Fig. 2b).

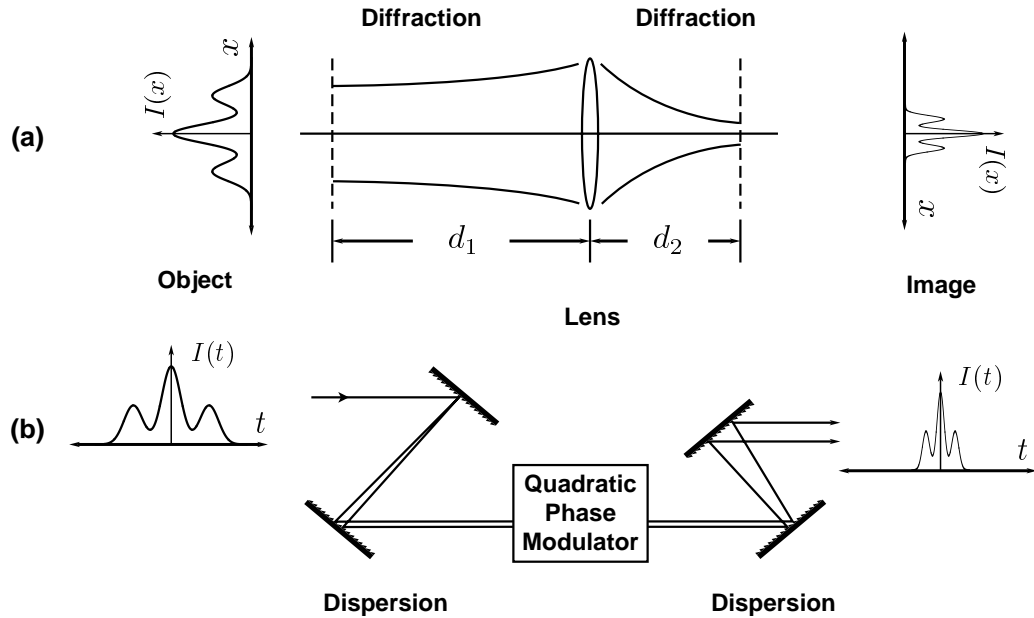


Figure 2. A comparison of temporal imaging (a) and spatial imaging (b). A quadratic phase modulator is used as a time lens while dispersion and diffraction play equivalent roles.

The missing element is the time analog of a lens; a “time lens” or something

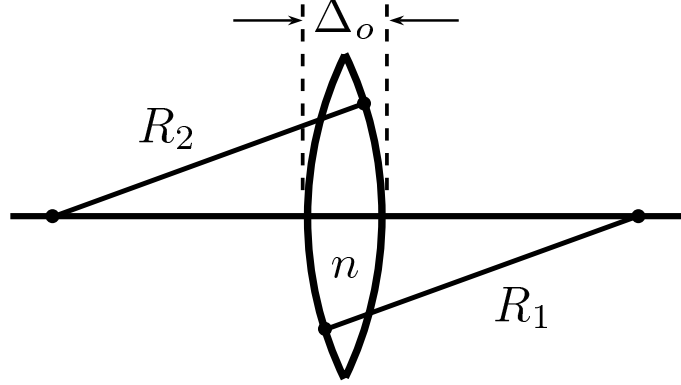


Figure 3. Diagram of a thin lens showing the essential physical properties. Index, n ; thickness, Δ_0 ; surface curvatures, R_1 and R_2 .

like it. To develop this concept, let us first look at the spatial case in which a thin lens, as shown in Fig. 3, produces a phase transformation in real space of the form [9]

$$t_l(x, y) = \exp [ikn\Delta_0] \exp \left[-i \frac{k}{2f} (x^2 + y^2) \right], \quad (29)$$

where the first exponential term is a static phase shift and the second term represents a quadratic approximation to a spherical phase surface (paraxial approximation). The amount of curvature imparted to an incident wave is dependent on the wavenumber, k , and a scaling factor f called the focal length, which is assigned the following definition

$$f \equiv \frac{1}{(n-1) \left(\frac{1}{R_1} - \frac{1}{R_2} \right)} \quad (30)$$

Thus the lens “strength” is a function of the material index, n , and the surface curvatures, R_1 and R_2 . Going back to Eq. (29), we see that a plane wave incident on a lens is transformed into either a converging or diverging spherical wave depending on whether f is positive or negative (respectively). It is the action of the *quadratic* phase by the lens, along with subsequent propagation, or diffraction,

which allows us to form spatial imaging systems. Therefore, in the time domain, we must be able to impart a temporal quadratic phase onto optical waveforms when forming a temporal imaging system.

1.2 Electro-Optic Phase Modulation

One way of attaining quadratic phase modulation on an optical signal is to use electro-optic phase modulation. To understand this method we need to go back to the basic theory underlying the operation of electro-optic modulators (EOM). An EOM employs the Pockels effect, an electric field induced change in the index of refraction. For many materials, this index change is linear with the applied external electric field. Therefore, if a sinusoidal electric field is applied to the material, there will be regions of no index change at the nodes and regions of maximum index change at the cusps. It is the cusp regions that are of greatest interest, for if we apply a Taylor series expansion we find that the electric field variation near the maxima is quadratic.

To illustrate the point, let us assume a time-invariant electric field of the form $E(x, t) = E \cos(kx)$. If we expand the cosine, using

$$\cos(u) \approx 1 - \frac{u^2}{2!} + \frac{u^4}{4!} - \dots, \quad (31)$$

then the field at a cusp, i.e., small argument, can be approximated by

$$E(x, t) \approx E_0 \left[1 - \frac{(kx)^2}{2} \right]. \quad (32)$$

Due to the Pockels effect, we get a quadratic change in the index. Thus, if the electric field is a traveling wave within the material, an optical pulse copropagating within a cusp (Fig. 4) will experience quadratic retardation, which is equivalent to linear frequency chirp [6].

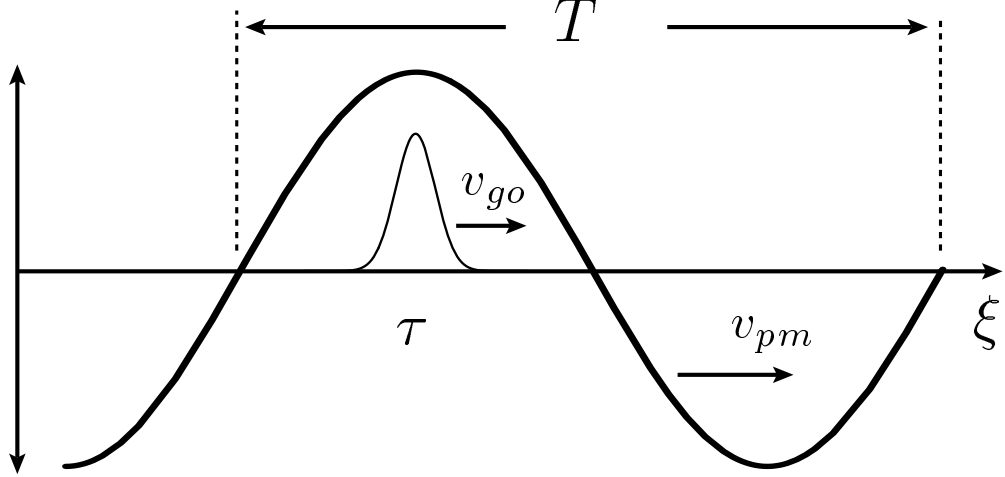


Figure 4. Illustration of an optical pulse copropagating with a microwave (RF) electric field. The RF field has a phase velocity of v_{pm} and a period of $T = 2\pi/\omega_m$. The optical pulse propagates with a group velocity of v_{go} .

The amount of phase modulation is dependent on many factors, including the strength of the electric field, the strength of the electro-optic coefficient, and the total interaction length. Another important parameter is the phase matching between the optical group velocity and the RF phase velocity. If these are not exactly matched, the optical pulse will exhibit “walkoff”. In other words, the pulse will slip away from the RF cusp as they propagate through the media, causing higher order phase modulation in the pulse. To determine a more specific relationship, it is necessary to develop the path integral which describes the action of an EOM on a propagating optical pulse [6].

An optical wave propagating through an electro-optic crystal (applied field $v(t) = V_0 \cos \omega_m t$) with a traveling-wave index $\Delta n(z, t)$, acquires a total phase shift given by

$$\begin{aligned} \phi(z, t) &= \omega_0 t - k_0 z - \frac{\omega_0}{c} \int_0^z \Delta n(z', t) dz' \\ &= \omega_0 t - k_0 z - \Gamma(z, t), \end{aligned} \tag{33}$$

where $\Gamma(z, t)$ represents the phase retardation due to the electro-optic interaction with the microwave field. The traveling-wave index can be expressed as

$$\Delta n(z, t) = \Delta n_0 \cos(\omega_m t - \beta_g t + \theta). \quad (34)$$

Here, Δn_0 is the peak index change for the applied peak electric field and the particular electro-optic coefficients, ω_m is the microwave frequency, β_g is the guided microwave propagation constant, and θ is an initial phase offset.

By casting the integral (33) into the traveling-wave coordinate system of (24), the results will be more easily interpreted. Thus, the path integral for the net retardation due to the electro-optic interaction is

$$\begin{aligned} \Gamma(\xi, \tau) &= \frac{\omega_0}{c} \int_0^\xi \Delta n(\xi', \tau) d\xi' \\ &= \frac{\omega_0}{c} \int_0^\xi \Delta n_0 \cos \left[\omega_m \left(\tau + \xi' \left(\frac{1}{v_{go}} - \frac{1}{v_{pm}} \right) + \frac{\theta}{\omega_m} \right) \right] d\xi'. \end{aligned} \quad (35)$$

This evaluates to

$$\Gamma(\xi, \tau) = \Gamma_0 \frac{\sin\left(\frac{\Delta\phi}{2}\right)}{\left(\frac{\Delta\phi}{2}\right)} \cos\left(\frac{\Delta\phi}{2} + \omega_m \tau + \theta\right), \quad (36)$$

where

$$\Delta\phi = \omega_m \xi \left(\frac{1}{v_{go}} - \frac{1}{v_{pm}} \right) \quad (37)$$

is the phase shift due to velocity mismatch between the optical group and microwave phase velocities. Γ_0 is the peak phase deviation in the absence of velocity walkoff and is defined by

$$\Gamma_0 = \frac{\omega_0 \Delta n_0 \xi}{c}. \quad (38)$$

The phase offset term θ in (36) allows us to insure that the pulse only acquires quadratic phase, even if a velocity mismatch is present. This can be explained in the following manner; if the pulse enters the RF field with an offset of $\theta = -\Delta\phi/2$, as the optical pulse and electric field propagate, the pulse begins to “slide” through the cusp of the RF. At a distance $\xi/2$ it will be centered under the cusp. After propagating the rest of the distance, the pulse exits the RF field. Thus, the pulse spent the same amount of time (or distance) on each side of the cusp center. Since the slopes on each side of the cusp are opposite in sign, any linear phase modulation acquired during the first half of propagation is canceled during the second half. This also results in a reduction of the total quadratic phase retardation due to the sinc-like term in (36).

The above analysis applies only to the case of traveling-wave modulators with copropagation of the optical and RF fields. However, it turns out that in the instance of resonant modulation, the counterpropagating wave will not effect the total modulation if the resonator is an integral number of half-wavelengths long and v_{pm} and v_{go} are equal. In effect, the modulation of the backward traveling-wave is “washed out” when the optical pulse passes through it [6].

Focal Time

Without loss of generality, we will assume an initial phase offset of zero and complete velocity matching between v_{pm} and v_{go} . Equation (36) now reduces to $\Gamma(\xi, \tau) = \Gamma_0 \cos(\omega_m \tau)$, and when expanded about $\tau=0$ using Eq. (31) we get

$$\Gamma(\xi, \tau) = \Gamma_0 \left[1 - \frac{(\omega_m \tau)^2}{2} \right]. \quad (39)$$

From this, the phase transformation in time becomes

$$h_{tl}(\tau) = \exp[-i\Gamma_0] \exp\left[i\frac{\omega_0}{2f_T}\tau^2\right], \quad (40)$$

where f_T , the “focal time”, is defined as

$$f_T \equiv \frac{\omega_0}{\Gamma_0\omega_m^2}. \quad (41)$$

Just as in the spatial case, Eq. (29), the first exponential term in (40) is a static phase shift corresponding to the delay through the “center” of the lens. The second term contains the scaling factor, or focal time, which determines the amount of curvature or quadratic phase modulation imparted to the optical waveform. There is a more general form for the focal time than that shown in Eq. (41). It can be used to describe any quadratic phase regardless of how it is generated and is defined in terms of the induced chirp rate $d\omega_i/dt$ [10]:

$$f_T = \frac{\omega_0}{d\omega_i/dt}. \quad (42)$$

This shows that the fundamental criterion for a strong time lens is maximizing the chirp rate it induces on the waveform under observation.

If we want to know the amount of frequency chirp or sweep that is imparted to the pulse, we can take the second derivative of the phase with respect to time, $d\omega/dt = d^2\phi/dt^2$. For an EOM, the imparted phase is $\Gamma(\xi, \tau)$, and if we maintain the earlier assumptions of phase matching and zero offset, the frequency chirp is expressed as

$$\frac{d\omega_i}{dt} = \Gamma_0\omega_m^2. \quad (43)$$

Thus, if we substitute (43) into (42) we again have the focal time of an electro-optic modulator,

$$f_T = \frac{\omega_0}{\Gamma_0 \omega_m^2}. \quad (44)$$

f -number and Resolution

There is one more parameter which should be introduced at this point: the temporal f -number, $f_T^\#$. In classical optics, the f -number ($f^\#$) determines the resolving power of an imaging system and is given by the ratio of focal length to aperture size. Equivalently, if we define a temporal aperture τ_a and define $f_T^\#$ to be the ratio of focal time to aperture size, we get

$$f_T^\# = \frac{f_T}{\tau_a} = \frac{\omega_0}{\tau_a (d\omega_i/dt)}. \quad (45)$$

If we think of the denominator as defining a fractional bandwidth $\Delta\omega = \tau_a (d\omega_i/dt)$, then (45) can be written as

$$f_T^\# = \frac{\omega_0}{\Delta\omega}. \quad (46)$$

Therefore, the temporal f -number is given by the inverse fractional bandwidth introduced by the lens.

We are also interested in finding out how the resolution of an imaging system is determined. However, we need to look at what conditions are necessary to form a reasonable “image” of the input waveform at the output of a system such as the one shown in Fig. 5. In the spatial case, the imaging condition is given by the lens law

$$\frac{1}{d_1} + \frac{1}{d_2} = \frac{1}{f}. \quad (47)$$

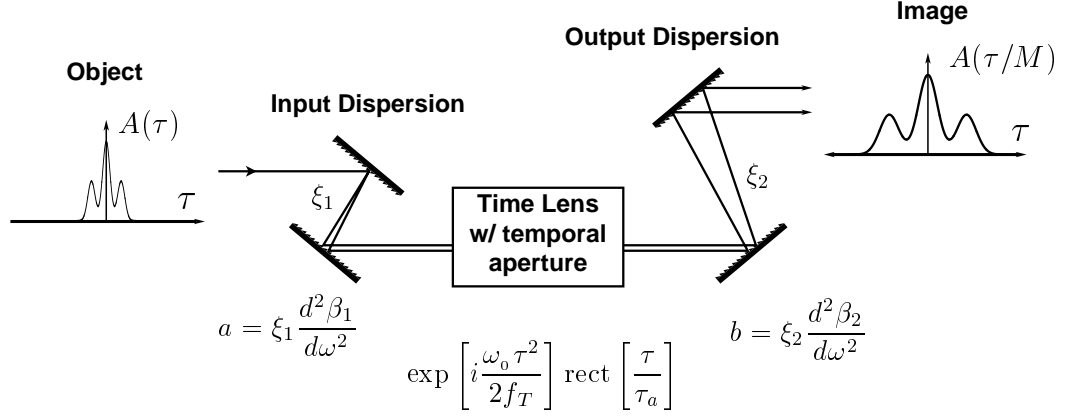


Figure 5. Temporal imaging configuration for a time microscope. a and b are the input and output dispersions, respectively. The time lens includes a temporal aperture with a duration τ_a , and the system magnification is $M = -b/a$.

It has been shown [6] that the equivalent temporal imaging condition is given by

$$\frac{1}{\xi_1 \frac{d^2 \beta_1}{d\omega^2}} + \frac{1}{\xi_2 \frac{d^2 \beta_2}{d\omega^2}} = -\frac{\omega_0}{f_T}, \quad (48)$$

where input and output distances in the lens law are replaced by dispersion. The minus sign results from differences in the governing differential equations for diffraction (14) and dispersion (26). When the imaging condition (48) is satisfied, the time scale is altered by a magnification factor, M , given by the ratio of output to input dispersions, i.e.

$$M \equiv -\frac{\xi_2 \frac{d^2 \beta_2}{d\omega^2}}{\xi_1 \frac{d^2 \beta_1}{d\omega^2}}. \quad (49)$$

This expression also has its analog in the spatial domain, where the magnification equals the ratio of the image distance to the object distance ($-d_2/d_1$).

It is well known that the resolution of any imaging system is given by the Fourier transform of its aperture function. This also applies to temporal imaging systems [6]. Consider a temporal imaging system, say a time microscope, with a

rectangular time aperture, or pupil function, τ_a in duration (Fig. 5). Just as in the spatial case, the impulse response of this system will be a magnified replica of the input waveform convolved with the Fourier transform of the pupil function. In the case of a rectangular aperture, the pupil function transforms to a sinc function. If we have a system with magnification, M , the impulse response takes the form [6]

$$I(\tau - \tau'_0) = \frac{\tau_a}{4\pi b\sqrt{M}} \exp\left[\frac{i\omega_0\tau^2}{2Mf_T}\right] \text{sinc}\left(\frac{\tau_a(\tau - \tau'_0)}{4\pi b}\right), \quad (50)$$

where a and b are

$$a = \xi_1 \frac{d^2\beta_1}{d\omega^2} \quad \text{and} \quad b = \xi_2 \frac{d^2\beta_2}{d\omega^2}. \quad (51)$$

From (50), the resolution can be roughly estimated by using the first zero of the sinc function as a marker. This corresponds to an output time interval of $(\tau - \tau'_0) = 4\pi b/\tau_a$. Using the magnification ratio, we can translate this to an input time scale. Thus, the input resolution, or the smallest resolvable input time feature, is

$$\delta\tau_{in} = \left| \frac{4\pi b}{M\tau_a} \right| = \frac{4\pi a}{\tau_a}. \quad (52)$$

In a spatial microscope, the magnification is generally large and the image distance is much greater than the object distance. Thus we approximate the object distance to equal the focal length. For a temporal microscope, this implies that the output dispersion is much greater than the input dispersion, and $a \approx -f_t/\omega_0$. Consequently, from (46) and (52) the minimum resolvable time feature is given by

$$\delta\tau_{in} = T_0 f_T^\# = \frac{1}{\Delta f}, \quad (53)$$

where T_0 is the optical carrier period and Δf is the fractional bandwidth generated by the time lens. This is an interesting result. It indicates that the resolution of

a temporal imaging system depends *only* on the fractional bandwidth imparted to the optical waveform by the time lens.

Let us consider the special case of the EOM. Quadratic phase modulation is obtained only during part of the RF cycle. It was found in previous studies of active pulse compression that the useful temporal aperture can be approximated by [11]

$$\tau_a \approx T/2\pi = 1/\omega_m \quad (54)$$

where ω_m is the angular modulation frequency. If this is used in conjunction with Eq. (44) then the temporal f -number for an EOM reduces to

$$f_T^\# = \frac{f_T}{\tau_a} = \frac{\omega_0}{\Gamma_0 \omega_m}. \quad (55)$$

From this, we get an expression for the EOM resolution

$$\delta\tau_{in} = T_0 \frac{\omega_0}{\Gamma_0 \omega_m} = \frac{1}{\Gamma_0 f_m}. \quad (56)$$

With this expression we can define the performance of a time lens within an imaging system based only on its peak phase deviation and the modulation frequency.

Electro-Optic Time Lenses

2

The previous chapter described how an electro-optic phase modulator can be used as a time lens. Although the concept is fairly simple and straightforward, the design and construction of a practical, or strong, lens is neither. The extent of “parameter space” within time lens design is immense and largely unexplored. These parameters include modulation frequency, electro-optic materials, the type of RF structure, pulsed or continuous operation, type of crystal/structure cooling, optical configuration, and many, many more. However, from Eq. (36) we know that in order to make a strong lens we must have large electric fields and long interaction lengths. But, there are some very practical limitations on both of these quantities. Large electric fields can result in heating of the electro-optic material causing thermal lensing or thermally induced crystal stresses or in the extreme case, large electric fields may cause material breakdown. Long interaction lengths typically indicate more material, which increases costs. But even if cost were not an issue, many electro-optic materials are not available in large sizes due to difficulties in growth. These are only a few of the obstacles involved with implementing a useful time lens; many more will be covered in the following sections. In this chapter we will investigate the design, construction and characterization of a practical time lens.

2.1 Design Considerations

There are three major considerations when designing an electro-optic modulator: RF, mechanical, and thermal. All of these are influenced by outside factors including cost, complexity of design, and availability of materials, which are all interdependent. So, any design path we take will be iterative and contain many compromises, but when we are finished we will have at least one solid “coordinate” in parameter space.

RF Design

As a proof of principle, a temporal imaging system was designed to demagnify (compress in time) optical pulses. The source of the optical pulses was a Coherent Antares actively mode-locked Nd:YAG laser. The laser produced 75–90 ps pulses at a repetition rate of 80 MHz and a wavelength of 1.064 μm . Since pulse compression does not require a variable temporal aperture, we took advantage of a resonant cavity design. Using a resonant structure for the modulator [12], instead of a traveling wave structure [11], yields a considerable increase in the electric field for a given applied RF power. The drawback to this approach is that it restricts the versatility of the lens since the usable aperture is now fixed in duration ($\Delta\tau_{\text{aperture}} \approx 1/\omega_m$). However, this should not be a problem for our particular application. Now, a temporal aperture of at least 90 ps is necessary to stay within the quadratic region of the sinusoid (Eq. (54)). This mandated a maximum modulation frequency of 1.77 GHz to avoid aberrations.

Before going any farther in the RF design, I had to choose the electro-optic material used in the modulator. There were many different factors involved in making the best decision; however, we already had several pieces of lithium niobate

(LiNbO₃) available. Therefore, I will discuss the many material choices available later in this chapter and will proceed with the particular design at hand. Lithium niobate has a relatively large electro-optic coefficient, $r_{33} = 30.8$ pm/V at 632.8 nm, and its RF properties are fairly well known up to 10 GHz. Its loss tangent ($\tan \delta$) [13] is below 0.05 at 2 GHz, but it has a relatively high dielectric constant of $\epsilon_r \sim 28$ ($\sqrt{\epsilon_r} = 5.3$). Since the optical signal sees an index of $n_e = 2.1561$, it was a little challenging to match the optical group and RF phase velocities.

Velocity Matching

As was discussed in Section 1.2, the optical pulse must copropagate with the RF field for the maximum modulation to occur. If there is a velocity mismatch, then the total modulation will be reduced with a sinc-like functional dependence

$$\Gamma(\xi, \tau) = \Gamma_0 \underbrace{\frac{\sin\left(\frac{\Delta\phi}{2}\right)}{\left(\frac{\Delta\phi}{2}\right)}}_{\substack{\text{velocity} \\ \text{mismatch} \\ \text{term}}} \cos\left(\frac{\Delta\phi}{2} + \omega_m \tau + \theta\right), \quad (57)$$

where $\Delta\phi$ is the amount of phase shift between the optical and microwave fields and is defined below. The condition for perfect velocity matching $v_{go} = v_{pm}$ yields

$$\Delta\phi = \omega_m \xi \left(\frac{1}{v_{go}} - \frac{1}{v_{pm}} \right) = 0 \quad (58)$$

and implies an *ideal guided* microwave propagation constant (one which gives perfect velocity match)

$$\beta_{g_{ideal}} = \frac{\omega_m}{v_{go}} \approx \frac{\omega_m n_{\text{xtal}}}{c}, \quad (59)$$

where n_{xtal} is the index of refraction for the crystal. Thus, the waveguide or resonant structure used for the EOM would need to have a guided propagation constant as

close to $\beta_{g_{ideal}}$ as possible. Table 1 shows the different values of $\beta_{g_{ideal}}$ for multiples of the laser repetition rate (80 MHz) near 1.7 GHz as calculated from (59). This is important, for if the EOM propagation constant β_g is exactly matched to $\beta_{g_{ideal}}$, then the optical and RF fields will copropagate for *any* interaction length.

Modulation Frequency (GHz)	$\beta_{g_{ideal}}$ (m^{-1})
1.52	68.6865
1.60	72.3016
1.68	75.9167
1.76	79.5318
1.84	83.1469
1.92	86.7620
2.00	90.3770

Table 1. The guided RF propagation constants necessary for perfect velocity matching of the optical pulse and the traveling microwave field for modulation frequencies near 1.7 GHz.

For a given length of crystal placed inside a waveguide resonator, the guide wavelength λ_g must be related to the crystal length ℓ according to

$$\lambda_g = \frac{2\ell}{n} \quad n = 1, 2, 3, \dots \quad (60)$$

where n is the integer mode number. Consequently, the crystal length must be an integer multiple of guided half-wavelengths to make the structure resonant. The *guided* propagation constant β_g depends on the mode according to

$$\beta_g = \frac{2\pi}{\lambda_g}. \quad (61)$$

For our EOM we chose a TE_{101} ($n = 1$) mode for several reasons. First, the electric field nulls are at the walls of the cavity making it possible to utilize

the whole crystal cross-section for modulation. Second, and more importantly, the guided propagation constant is very close to the one required for perfect velocity matching as shown below.*

<u>TE₁₀₁</u>	<u>TE₁₀₂</u>
$\lambda_{g_{101}} = 40 \text{ mm} \times 2 = 80 \text{ mm}$	$\lambda_{g_{102}} = 40 \text{ mm} \times 1 = 40 \text{ mm}$
$\beta_{g_{101}} = \frac{2\pi}{\lambda_{g_{101}}} = 78.5398 \text{ m}^{-1}$	$\beta_{g_{102}} = \frac{2\pi}{\lambda_{g_{102}}} = 157.080 \text{ m}^{-1}$

Referring to Table 1 we see that the frequency 1.76 GHz corresponds to a propagation constant very near the result obtained for the TE₁₀₁ mode. The residual velocity mismatch results in a phase shift

$$\begin{aligned} \Delta\phi &= \xi (\beta_{g_{ideal}} - \beta_{g_{101}}) \\ &= 40 \text{ mm} (79.53 \text{ m}^{-1} - 78.54 \text{ m}^{-1}) = 0.0397 \text{ rad} \end{aligned}$$

and a corresponding reduction in phase modulation (36)

$$\frac{\sin\left(\frac{\Delta\phi}{2}\right)}{\left(\frac{\Delta\phi}{2}\right)} = 0.99974.$$

Thus, there was less than a 0.03% reduction in the total phase modulation due to velocity mismatch. This calculation assumes that we injected the optical pulse with a phase offset equal to $\Delta\phi/2$ as explained in Section 1.2.

Resonator Design

At this point two parameters have been determined. The modulation frequency is 1.76 GHz and the resonator length is 40 mm, supporting a TE₁₀₁ mode. Next, I designed the resonator geometry. At first, it might seem that a simple approach

* $\lambda_{g_{lmn}}$ is the guided wavelength for a particular resonant mode lmn . The guided propagation constant for the mode lmn can then be calculated from $\lambda_{g_{lmn}}$.

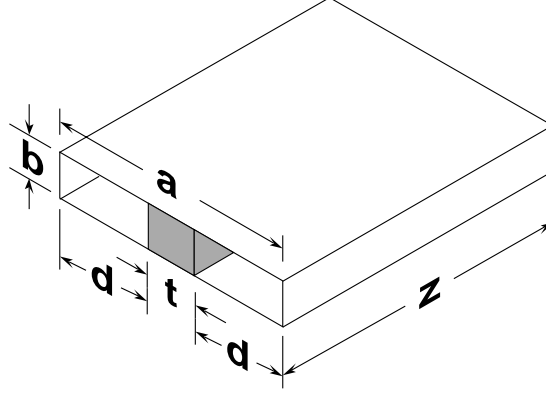


Figure 6. Simplest possible configuration for resonant electro-optic modulator. For our crystal the a dimension would have to be 93.6 mm in order to obtain the correct guided wavelength.

is to place the crystal in a rectangular waveguide cavity to form a partially loaded waveguide resonator, as shown in Fig. 6. Let us explore this design.

The resulting eigenfunctions and propagation constants for the cavity configuration shown in Fig. 6 are given below. The eigenvalue equations for a symmetrically placed dielectric slab in rectangular waveguide are [14]

$$l \tan hd = -h \tan \frac{lt}{2} \quad (\text{asymmetrical modes}) \quad (62)$$

$$h \cot hd = l \tan \frac{lt}{2}, \quad (\text{symmetrical modes}) \quad (63)$$

where l and h are the wavenumbers for the dielectric and air regions, respectively, and must satisfy the relation

$$\beta_g^2 = l^2 + \left(\frac{m\pi}{b}\right)^2 - \epsilon_r k_0^2 = h^2 + \left(\frac{m\pi}{b}\right)^2 - k_0^2, \quad (64)$$

where k_0 is the free space propagation constant $k_0 = \omega\sqrt{\mu_0\epsilon_0}$. In order to find a solution, we substitute (64) into (63) and solve the transcendental equation numerically. Given the TE_{101} mode ($m = 0$), $\beta_g = 78.539 \text{ m}^{-1}$, and a modulation frequency of 1.76 GHz, we can solve for d (or a). The calculated value of a is quite

large, 93.6 mm. This gives an aspect ratio of 23:1 (a:b). This leads to an unreasonably large structure (compared to the crystal), which in turn increases costs for machining, gold plating, etc. Also, the RF fields would not be as well confined to the crystal when compared to other possible resonator structures.

To resolve these issues, let's look at other waveguide/resonator geometries. One configuration, ridge waveguide, has some attributes which make it a good alternative (Fig. 7). The presence of the ridge lowers the cutoff frequency of the dominant mode in the guide, allowing the use of a smaller aspect ratio. Also, for symmetric modes, the electric field tends to be concentrated in the gap region. If the dielectric is placed in this region, there is a significant increase in the electric field across the crystal for a given input RF power.

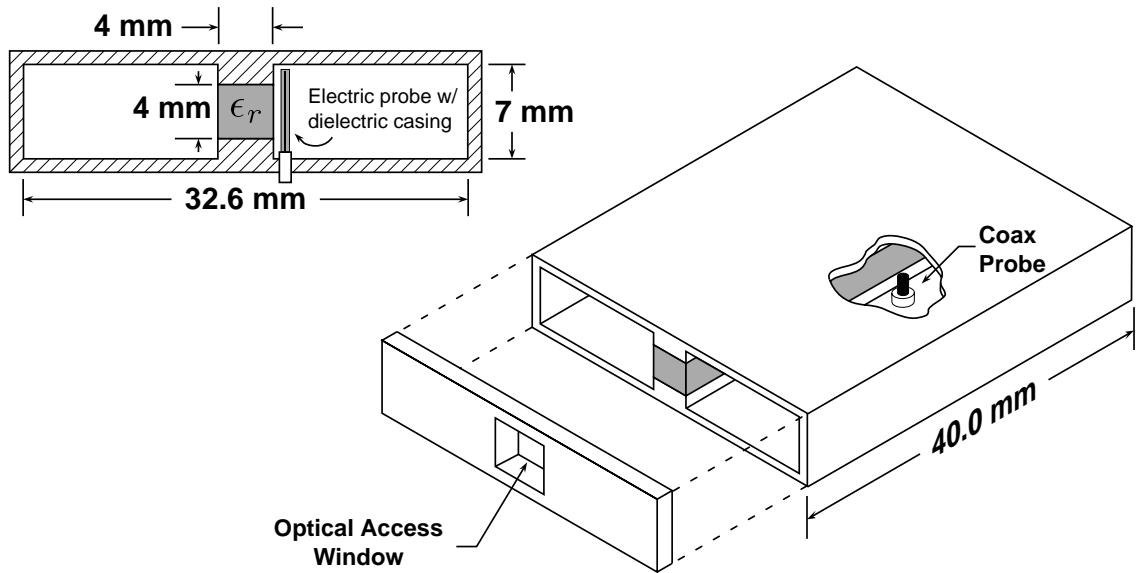


Figure 7. Partially loaded ridge waveguide resonator used as an electro-optic modulator. The resonant frequency is 1.76 GHz and $\beta_g=78.539 \text{ m}^{-1}$. Note: the ends of the resonator are capped except for a hole in front of the crystal for optical access.

One of the drawbacks to using this configuration is the difficulty in obtaining a closed form solution for the eigenfunctions and propagation constants. Many

approximate expressions have been published in the literature [15–17], but none of these treat the case of partial dielectric loading.

To obtain an accurate estimate of the field configuration, I used a 3D electromagnetic field modeling program called HFSS (High Frequency Structure Simulator) running on a high-speed workstation. This program calculates the eigenvalues and propagation constants for almost any structure. However, HFSS is an analysis tool, not a synthesis tool. Therefore, I used the rectangular waveguide solution as a starting point for the analysis. By adding a small double ridge and decreasing the value of a in successive runs, I was able to extrapolate the correct dimensions for the waveguide in order to get $\lambda_g = 80$ mm. This analysis was done using only a ridged waveguide model, not the full resonant structure. The waveguide runs would take on the order of 20–30 minutes. Simulation of the whole resonant structure took in excess of 5 hours. However, this modeling was necessary to determine the effect on the resonant frequency of the dielectric tuning, the coaxial probe, and the apertures at the crystal faces.

Full simulations of the resonator indicated that the electric field would be approximately 1×10^4 V/m at the peak with 1 Watt of RF power. Using this and Eq. (38), where $\Delta n_0 \simeq n_0^3 r_{33} E_z / 2$, gives $\Gamma_0 = 0.36$ rad/ \sqrt{W} . This does not seem very large at first, but in these simulations, the coax coupling was not optimized and not all of the RF energy was injected into the resonator. Unfortunately, limited access to the computer prevented further investigation of these estimates.

Mechanical Considerations

How do you make a ridge-waveguide resonator with a loaded Q greater than 1000 which holds an electro-optic crystal between the ridges without stressing it,

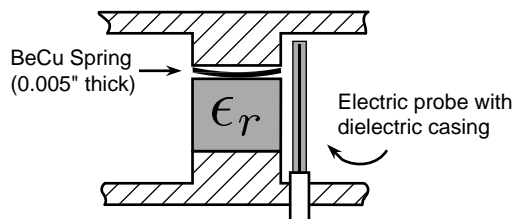


Figure 8. A close up view of the beryllium copper (BeCu) spring showing its placement in the ridge waveguide resonator. The 0.008" gap between the crystal and top ridge compressed the spring from its relaxed height of 0.01", thereby holding the crystal in place.

yet makes solid enough contact to conduct away heat? This was one of the more challenging questions that had to be answered during the mechanical design of the structure. First, I decided to use a solid piece of aluminum and have the lower half of the structure machined out, forming an open-topped box with a ridge along the bottom. Aluminum was used because of its good machinability, low cost, and, with a coating of nickel, its ability to be gold plated. A top piece containing only a flat surface and the top ridge was then attached to the bottom piece. Thus, the crystal was sandwiched between the two ridges when the pieces were screwed together. The mounting stress applied to the crystal was controlled by a beryllium-copper (BeCu) flat spring, which was placed between one of the ridges and the crystal (Fig. 8). BeCu has excellent electrical and thermal conductivity as well as the ability to hold a formed shape. After experimenting with many types of spring shapes, leaf with the bend transverse to long axis, wavy, and finally parallel leaf with the bend parallel to long axis, I found that the latter gave the best performance (lowest capacitance, highest Q , etc.) as data later in this chapter will show. The spring itself was approximately 0.005" thick (thickness with bend was approx. 0.01") and fit in an 0.008" gap between the crystal and ridge, Fig. 8. This left a small air-gap along the length of the ridge, which caused a slight change in reactance and altered

the resonant frequency slightly.

The amount of stress applied to the crystal was checked indirectly using a HeNe laser. If the compression of the crystal became very large when the top piece was screwed down, a HeNe beam passing through the crystal would be distorted due to stress-induced index changes. This was easily seen when the spring was made from thicker stock or was bent to a thickness greater than $\sim 0.011''$.

Thermal Considerations

With available microwave sources, we anticipated coupling in excess of 30 Watts of RF power. If the resonator is dielectric-loss-limited, as was the case, then nearly all of the RF power will be dissipated as heat in the $4 \times 4 \times 40$ mm crystal. LiNbO_3 is capable of operating at temperatures in excess of 400°C . Unfortunately, at temperatures above 200°C the electro-optic coefficient drops significantly ($>10\%$) and the loss tangent begins to increase. Thus, we had to get the heat out of the crystal at a rate which would allow it to stay below 200°C . This was accomplished by putting the top and bottom surfaces of the crystal in direct contact with the ridges and actively cooling the resonator. Regrettably, aggressive crystal cooling may lead to thermal gradients within the crystal, which could result in a nonuniform index of refraction (Section 2.3).

Another related thermal issue involves the resonant frequency of the cavity. As the temperature of the cavity changes, the resonant frequency drifts away from 1.76 GHz. If Q_L is greater than 1000, then it has a 3 dB resonance width of less than 2 MHz. Therefore, if the temperature drifts enough to change the resonance 1 MHz, the cavity reflects nearly half (15 Watts) of the input power back to the RF amplifiers.

In order to avoid this, I designed a temperature stabilization scheme. Initial results indicated it would be necessary to hold the temperature constant to better than $\pm 1^\circ\text{C}$ over the entire RF operating range of 0–30 Watts. In addition, both heating and cooling were deemed necessary to maintain a constant temperature over the range of 0–30 Watts. Thus, two high power resistors were mounted on the resonator case to act as heating elements and cooling was provided by a small water manifold also attached to the resonator housing. A thermistor imbedded in one of the ridges of the resonator gave an indication of the temperature. An instrumentation-type opamp circuit was then used to compare the temperature read by the thermistor against a reference voltage with the difference voltage controlling the current going to the resistor pair. Thus, the temperature change in the resonator was compensated by the heat load put out by the resistor pair (100 W capability). The final system was able to keep the temperature stable to within $\pm 0.7^\circ\text{C}$ over the operating range of the resonator.

2.2 Construction

Machining of the modulator was facilitated by the use of CAD/CAM tools and a CNC machine. Tolerances for most of the dimensions were $\pm 0.002''$, with the ridge separation being the most critical at $\pm 0.0005''$. Preparing the interior finish of the resonator required painstaking attention to detail. The aluminum had to be polished to improve surface conductivity, but care had to be taken not to round off the edges of the ridges or mating surfaces. After polishing, the resonator was first plated with $0.3\ \mu\text{m}$ of nickel to prevent “purple plague” [18], and then gold plated to a thickness of 3–3.5 μm (skin depth at 1.76 GHz = 1.9 μm). After final assembly the crystal was checked for stresses as described earlier.

During the final stages of construction, the resonant frequency was checked. The empty cavity frequency was within less than 0.25% of what HFSS had predicted. But, with the spring and crystal in place, the resonance was off by +18 MHz at 25°C, $\sim 1\%$. This could be due to small differences in the crystal size, dielectric constant, the anisotropic nature of LiNbO_3 , or the extra reactance of the spring.*

RF power was coupled into the resonator using an electric field probe made from 0.086" semi-rigid coax. The probe was inserted through the top of the resonator, next to the crystal and centered along the length (Fig. 7). This is where the electric field strength is the greatest. The amount of coupling was adjusted by changing the insertion depth of the probe via a small translation stage attached to the top of the resonator.

2.3 Modulator Characterization

The first step in characterization was to determine the RF properties of the cavity. Resonance frequency and cavity Q are two of the most important RF properties. The modulator had to be run at exactly 1.76 GHz in order to stay in phase with the pulses coming from laser. The cavity Q determines what peak electric field is generated for a given input power. The modulator was designed to have several means of tuning the resonant frequency. Dielectric tuning (tuning range ± 5.5 MHz) was accomplished using a sapphire rod (7 mm \times 3.8 mm diameter, $\epsilon_r \sim 9$) with a dielectric "puck" (3 mm \times 4 mm diameter, $\epsilon_r > 20$) attached to the end. The rod and puck were placed in the high electric field region near the crystal opposite the field probe, and the amount they protruded into the cavity could be changed

* HFSS is not capable of simulating the presence of the spring, since its dimensions are too small compared to the surrounding structure.

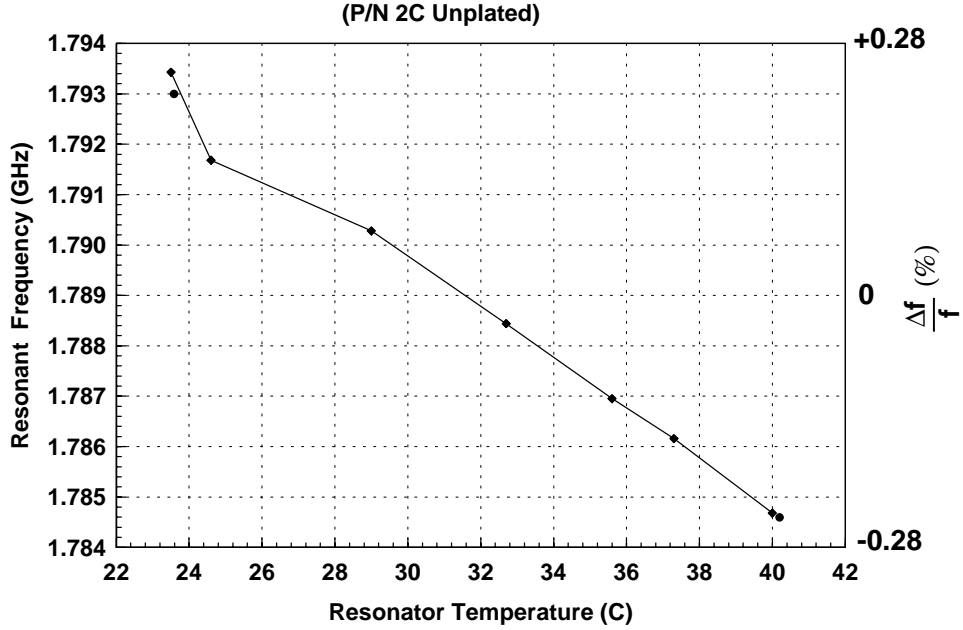


Figure 9. Resonant frequency as a function of temperature for the resonant phase modulator. The slope is 505 KHz/°C.

via an integral adjustment screw. Temperature tuning of the resonator gave the largest amount of frequency tuning, a total of 20 MHz tuning for a 25–60°C range at 505 KHz/°C. With the temperature tuning, it was possible to bring the resonance from 1.778 GHz down to 1.760 GHz when run at 60°C. Figure 9 shows the data on the temperature tuning of the *unplated* resonator. After plating the resonant frequency shifted slightly lower.

With the resonator at 50°C, the dielectric tuner was inserted until the resonance was shifted down to 1.76 GHz. The *loaded Q* (Q_L) of the resonator without the crystal or spring was 4,500 at 5.549 GHz. Q_L of the resonator with crystal and spring was 1,400 at 1.760 GHz.

To test the modulation index (Γ_0) of the resonator, I passed a HeNe laser beam through the modulator while applying an RF power of 500 mW and measured the

spectrum with a Fabry-Perot interferometer. The side-band *power* amplitude was 14% of the peak. Using a Bessel function expansion of the sinusoid and comparing the J_0 and J_1 functions with the field amplitude ratio ($\sqrt{\text{power amplitude}}$) I calculated a $\Gamma_0 = 0.59 \text{ rad}/\sqrt{\text{Watt}}$. Of course, this is for a *single* pass through the resonator at $\lambda = 0.6328 \mu\text{m}$. The modulation index will increase linearly with the number of passes. Chapter 3 will investigate multiple-pass configurations for the time lens and discusses its use in a pulse compression system.

2.4 Future Investigation

The development of electro-optic time lenses is in its infancy; especially the investigation of time lenses based on resonant structures. The major thrust of work should be in lowering the temporal f -number ($f_T^\#$) of the lens since this determines the minimum resolvable temporal feature (56). To put this in perspective, let us look at several different examples of modulators which could be used in a time microscope. Table 2 shows the resolution for a time microscope using EOM's with different modulation frequencies and peak phase deviations. Notice that in

Γ_0	f_m (GHz)	$\delta_{\tau_{in}}$ (ps)
25	20	2
100	20	0.5
25	50	0.8
100	50	0.2

Table 2. The minimum resolvable temporal feature size ($\delta_{\tau_{in}}$) for a time microscope using an EOM with various modulation frequencies and peak phase deviations.

order to obtain a resolution of 200 fs we would need a peak phase deviation of 100 rad at a modulation frequency of 50 GHz. This is not a trivial task. However,

new electro-optic materials, such as DAST*, with electro-optic coefficients 5 times that of LiNbO_3 are becoming available. These new materials in addition to new resonator geometries may make the requirements shown in Table 2 achievable.

* 4-dimethylamino-N-methylstilbazolium tosylate, a high-temperature organic nonlinear optical material with enhanced second-order properties.

Active Pulse Compression

3

Ever since the first pulsed lasers appeared in the early 1960's, applications have demanded shorter, higher power pulses. For many years, pulse characteristics were inherent in the design of the laser. A significant change in the output pulses required a new laser, resulting in the large variety of lasers that are available today. As early as the mid 1960's people began to explore ways of changing pulse characteristics, such as the pulse width, external to the laser [19, 20]. Soon experimental results in optical pulse compression were numerous and the drive for ever shorter pulses led to the record minimum pulse width of 6 fs obtained by Fork, et al. [21]. It is interesting to note that much of the early investigation of laser pulse compression evolved out of work done with chirped radar during the 1950's [22]. In this case radar pulses were stretched before amplification and transmission to reduce their peak power and then they were recompressed in the receiver. This allowed the radar pulses to have peak powers far above what the amplifiers could normally produce.

3.1 Self-Phase Modulation and Optical Pulse Compression

It is well known that for a given pulse shape the transform limited time-bandwidth product determines the minimum frequency bandwidth required to generate a specific pulse width. Therefore, to shorten the pulse, it must gain additional bandwidth in order to satisfy the time-bandwidth product. Generation of

the additional frequencies required to chirp an optical pulse for subsequent compression generally necessitates the use of nonlinear optical processes. Since the early 1980's the most common technique has been self-phase modulation (SPM), which is achieved simply by passing a pulse through an optical Kerr medium [23]. When an intense optical pulse is passed through a nonlinear medium, the refractive index, n , is altered by the optical electric field, E . Here we will define the optical field as $E(z, t) = A(z, t)e^{i[\omega_0 t - kz]}$ and the envelope function as $A(z, t) = E_0 e^{-\Gamma(z)t^2}$, where $\Gamma(z) = a - ib$ is the gaussian pulse parameter.* Thus, the index variation is

$$\begin{aligned} n &= n_0 + n_2 \langle E^2 \rangle + \dots \\ &= n_0 + n_{2_I} I + \dots, \end{aligned} \quad (65)$$

where n_0 is the linear index, n_{2_I} is the intensity second order nonlinear index, $\langle E^2 \rangle$ is the time average (with respect to carrier) of the squared electric field, and $I = \sqrt{\epsilon/\mu} \langle E^2 \rangle$. The net phase shift for the pulse when passing through a length ℓ of nonlinear medium will then be

$$\varphi(t) = (n_0 + n_{2_I} I) \frac{\omega_0 \ell}{c}, \quad (66)$$

and therefore the instantaneous frequency is

$$\omega_i = \frac{d\varphi}{dt} = \frac{n_{2_I} \omega_0 \ell}{c} \frac{dI(t)}{dt}. \quad (67)$$

If we assume an initially unchirped pulse for simplicity, and also the pulse shape $I(t)$ is not changed in passing through the length ℓ , then the instantaneous frequency becomes

$$\omega_i \approx \frac{4an_{2_I}\omega_0\ell I_0}{c} \times te^{-2at^2}. \quad (68)$$

* This is unrelated to the peak phase deviation Γ_0 .

This phase modulation creates a linear frequency chirp at the center of the pulse, as shown in Fig. 10. This frequency sweep can then be removed by a dispersive delay line, such as a diffraction grating pair, set to the value required for proper compression, or cancellation of the chirp.

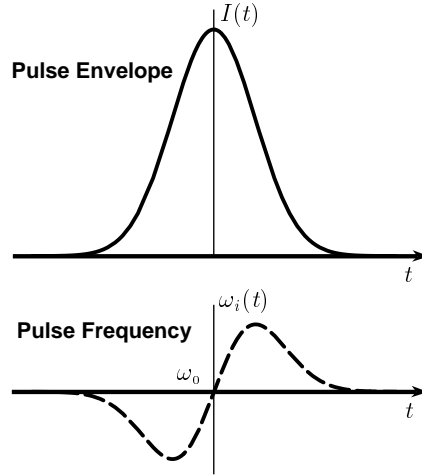


Figure 10. Self-phase modulation lowers the frequency on the leading edge of the pulse and raises the frequency on the trailing edge of the pulse because of its intensity dependent nature.

If there is significant group velocity dispersion (GVD), different portions of the pulse with slightly different optical frequencies will begin to travel at slightly different group velocities. This results in pulse shape changes as the distance traveled increases. Depending on the circumstances, this can lead to enhanced frequency chirping where the linear chirp region extends across most of the pulse [24].

Optical fibers are the most common Kerr media used in pulse compression [23, 24] since they confine the optical power to a small, well defined region, allowing large intensities to be achieved with relatively low power. But, the fiber generates undesired nonlinear effects if peak powers exceed more than a few hundred Watts. Also, because of the nature of SPM, undesired higher order modulation is present

in the pulse as it exits the fiber. This can be a problem since it can't be compensated by means of linear dispersive delay lines. Most significantly, fiber-grating compression is a noisy process by nature. If there are any fluctuations in the pulse envelope, whether in its width or peak power, they will considerably change those same characteristics of the compressed pulse. Finally, since the amount of chirp imparted to the pulse is determined by the pulse envelope, the useful power range for a desired pulse width is quite narrow.

3.2 Electro-Optic Pulse Compression

Fortunately, there is a much better way of obtaining pulse compression. It is related to the theory of temporal imaging described in Chapter 1. Recall that temporal quadratic phase modulation is equivalent to the behavior of a thin lens on a monochromatic beam in space (see Fig. 11). However, pulse compression, unlike true “imaging”, does not require input dispersion before the lens and its use would

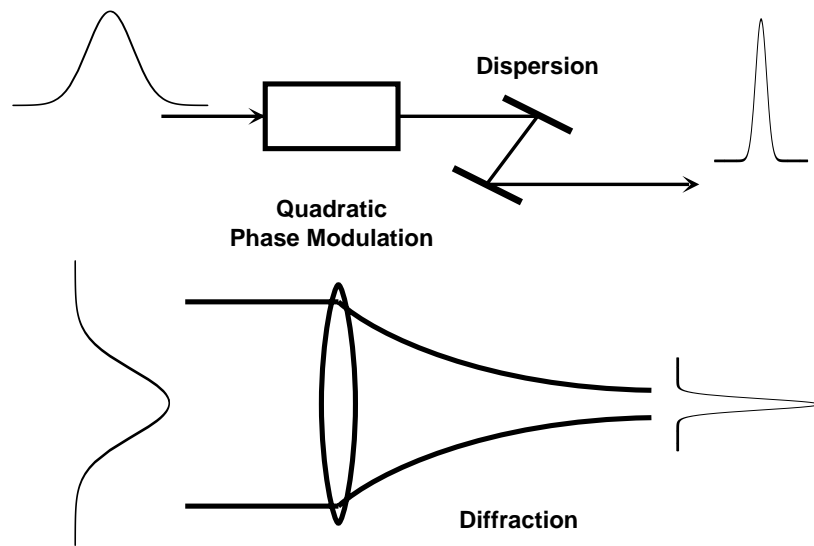


Figure 11. Optical pulse compression as the temporal analog of focusing a monochromatic beam. The role of the spatial lens is played by the quadratic phase modulator, ϕ_m , and free-space diffraction is replaced by dispersion in the form of a diffraction grating pair.

reduce the throughput efficiency of the compressor. The first demonstrations of pulse compression using electro-optic modulators, in conjunction with dispersive delay lines formed from resonant atomic vapor, were done more than two decades ago [25, 26]. More recently, this was demonstrated by Kolner [11] using a traveling-wave electro-optic phase modulator, and diffraction gratings and was designated *active pulse compression*.

Amplitude Noise

One of the most significant aspects of this type of pulse compression is the phase modulation's independence from optical pulse power. This is easily seen from Eq.'s (38) and (43) from Chapter 1:

$$\frac{d\omega_i}{dt} = \Gamma_0 \omega_m^2 \quad \dots \text{Modulator Chirp Rate} \quad (69)$$

$$\Gamma_0 = \frac{\omega_0 \Delta n_0 \xi}{c} \quad \dots \text{Peak Phase Modulation.} \quad (70)$$

Because of the independence from optical power, the relative amplitude noise of the optical pulse is not increased when compressed, unlike fiber-grating compressors.

Timing Jitter

Another important element of active pulse compression is the reduction of timing jitter. To understand this, let's look at the spatial analogy of active pulse compression using Fig. 12. In the absence of aberrations, if a beam of light (a) parallel to the optic axis is incident on a convex thin lens, it will pass through the optic axis at the focal point (f) of the lens. Now, if the beam is offset (b) from the optic axis it will still pass through the focal point although at some slightly different angle corresponding to a different spatial frequency. Thus, if the beam has jitter transverse to the direction of propagation before the lens, it will not have any

spatial jitter at the focal point. In this case, the spatial jitter has been transformed to angular (spatial frequency) jitter.

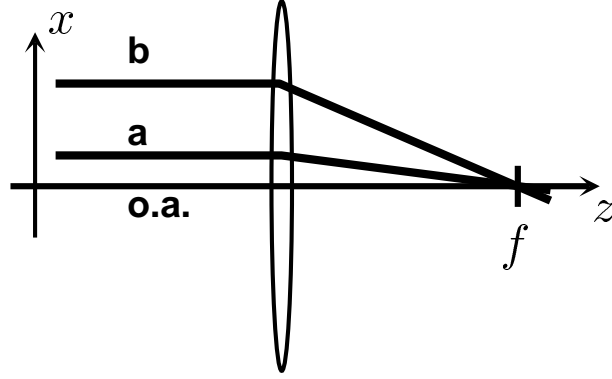


Figure 12. Effect of transverse beam jitter at the focal point (f). The transverse jitter before the lens becomes angular jitter at the focus.

Now, from the space-time analogy, the transverse variable, x , in the space domain corresponds to the local time variable, τ , in the time domain. And similar to the spatial case, any timing jitter in the pulse at the input of the compression system will be reduced to zero at the output (temporal focal point). Of course this only holds true if the system is aberration free and the dispersion is set to exactly cancel the phase modulation of the time lens. Timing jitter reduction does not occur in fiber-grating (passive) pulse compression because the reference frame for modulation is dependent on the pulse. i.e., the lens jitters with the pulse.

As in the spatial case, there are certain criteria which must be satisfied in order obtain an essentially aberration free system. The most basic criterion results from the assumption that only quadratic phase is acquired by an optical pulse if it is confined to a small region under the cusp of the microwave electric field. This region is defined in (54) and is approximately $T/6$, where T is the period of the microwave field. If the input pulse width exceeds this value, higher order terms

of the sinusoidal expansion become significant and linear dispersive delays will not completely compensate the phase. The spatial analogy to this is spherical aberration (except that the signs of the higher order terms alternate). This occurs when the paraxial condition is not satisfied and rays pass through portions of the lens which are not solely quadratic, thereby acquiring higher order phase modulation which results in a larger spot at the focus. References [11, 27, 28] show the effects of overfilling the time lens (RF cusp) on both the envelope and the timing jitter of the pulse.

“Single Knob” Adjustable Pulse Compression

In Chapter 1 we saw how a quadratic phase modulator can be used as a time lens, and Chapter 2 covered the construction and characterization of a resonant cavity EOM. This phase modulator still is not suited for use in an active compression system, because it has a single pass modulation efficiency of only $0.59 \text{ rad}/\sqrt{\text{W}}$. Even if we used 100 W of RF power to drive it, we would get only 5.9 rad of peak phase deviation. Using the expression for compression ratio,*

$$\frac{\tau_i}{\tau_o} = \sqrt{1 + \left[\left(\frac{\Gamma_o \pi^2}{\ln 2} \right) \left(\frac{\tau_i}{T} \right)^2 \right]^2}, \quad (71)$$

where the input pulse width τ_i is 85 ps and the RF period T is $1/1.76 \text{ GHz} = 568.2 \text{ ps}$, we get an output pulse width $\tau_o = 40 \text{ ps}$. This is a compression ratio of approximately 2:1, not very useful for most applications. However, we can significantly increase the modulation efficiency by multiple-passing of the laser beam through the EOM. If, for instance, it was possible to get 14 passes through the EOM, with 30 W of applied RF power we would get 45 rad of peak phase deviation. This would

* This expression, originally published in [11], is derived in Appendix A.

be enough to compress a pulse from 85 ps to less than 6 ps; a compression ratio of 14:1. A complete description of how a multiple-pass configuration was designed and built for the EOM is presented later in this chapter.

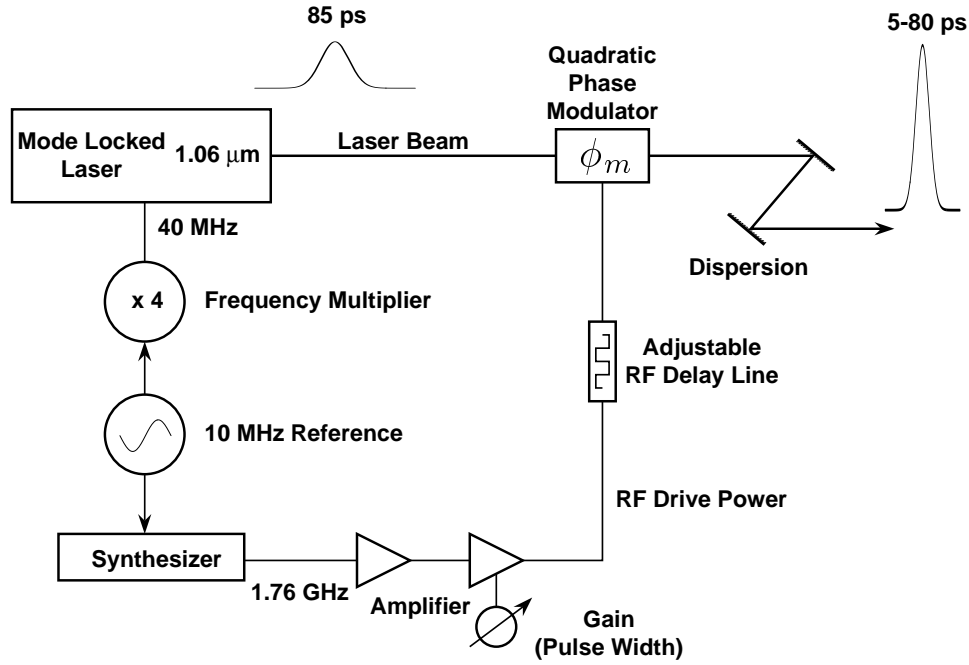


Figure 13. Schematic diagram of a basic active compression scheme showing the origin of the RF drive power and variability of the pulse width.

If we have the capability of obtaining large peak phase deviations ($\Gamma_0 > 25$), then it is possible to use active compression as a source of variable width picosecond pulses. Because Γ_0 is dependent on the RF drive power (through Δn_0), we can adjust the pulse width via a single knob, the RF power. A schematic diagram of how this might be done is shown in Fig. 13. A common reference frequency is necessary to phaselock the RF drive power and the pulses coming from the laser. The delay line is used to shift the phase of the RF so that the optical pulses enter the modulator under a cusp of the electric field.

Figure 14 demonstrates how the pulse characteristics will vary with changing

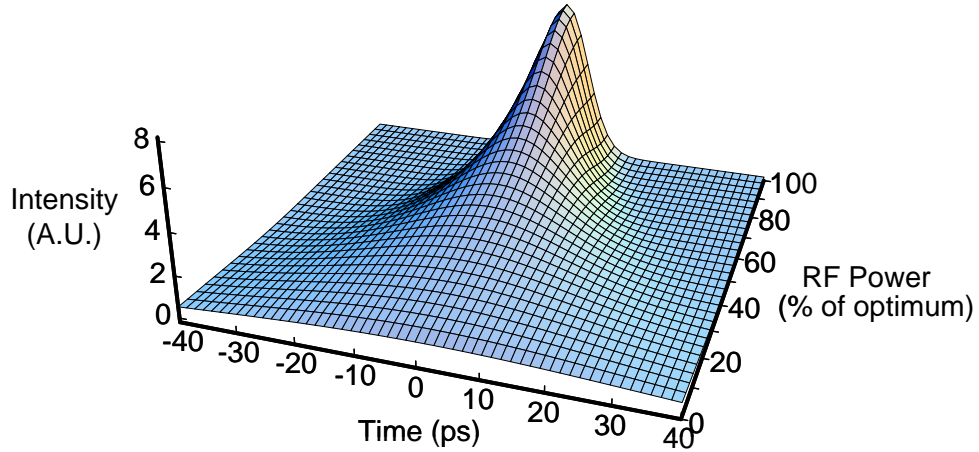


Figure 14. Theoretical example showing how a variation in RF drive power effects the output pulse of an active compression system. For this case f_{RF} is 1.76 GHz, τ_i is 85 ps, and Γ_0 is 25 radians at 100% RF power.

RF power when a configuration similar to the one shown in Fig. 13 is used. In this instance, the dispersion has been optimized for the minimum pulse width at the maximum RF power, which produces $\Gamma_0 = 25$ radians. The RF drive frequency is 1.76 GHz and the input pulse width is 85 ps ($\sim T/6$). With no RF power, the pulse is broadened by the dispersion to 87 ps (although this is not visible in the plot). As the power is increased to 100% the pulse compresses to a minimum of 8.5 ps. This yields a compression ratio of $\sim 10:1$.

The pulses coming from the compressor will be chirped if the RF drive power is reduced from the optimum (highest compression). For many uses, such as RF photocathode illumination and photoconductive switches, residual chirp is not a concern. If the application requires transform limited pulses, then the dispersion must be adjusted for each setting of RF drive power.

Another way of viewing how the active pulse compressor operates as a variable pulse width source is shown in Fig. 15. The performance of the compressor can be

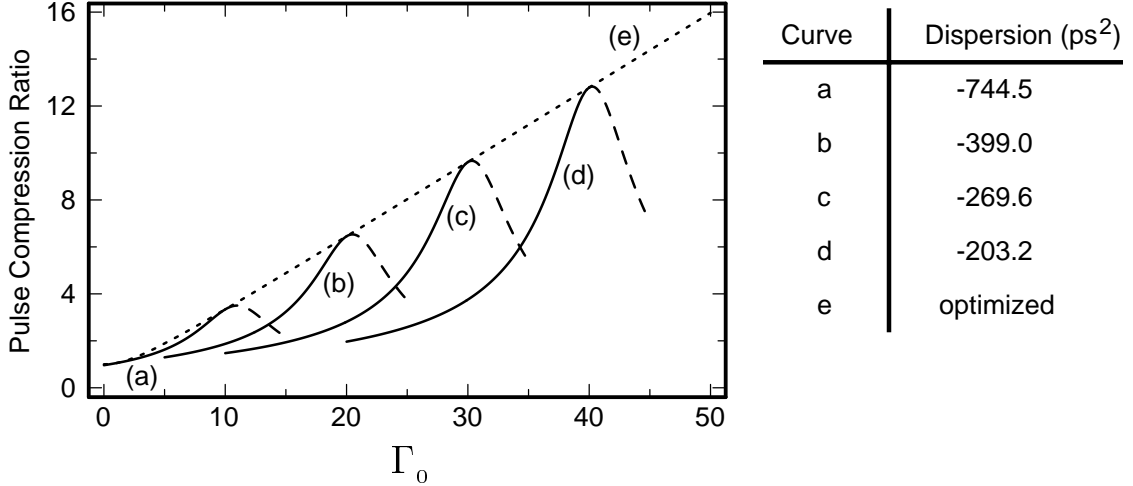


Figure 15. Theoretical plot of pulse compression ratio showing the dependence on peak phase deviation, Γ_0 . Curves (a-d) represent the compression ratio as function of Γ_0 and *fixed* values of dispersion. Curve (e) is the optimum compression ratio for Γ_0 and is described by Eq. (71). The drive frequency, f_{RF} , is 1.76 GHz, and the input pulse width, τ_i , is 85 ps.

optimized for a given value of Γ_0 by adjusting the dispersion to cancel the imparted chirp. The maximum compression ratio is shown by curve (e) and is a plot of Eq. (71) with $f_{\text{RF}} = 1/T = 1.76$ GHz and the input pulse width $\tau_i = 85$ ps. Curves a–d are plots of the compression ratio for varying peak phase deviation ($\propto \sqrt{\text{RF Power}}$) and a *fixed* value of dispersion. Notice that the compression ratio in curves a–d increases steadily from $\Gamma_0 = 0$ to the peak, but begins to decrease if you exceed the optimum compression point for a curve (i.e., increase Γ_0 beyond the optimum value of fixed dispersion). Also, the chirp of the pulse will change sign once Γ_0 exceeds the optimum value.

3.3 Design of a Multiple-Pass Optical Cavity

The application of a multiple-pass optical cavity to an electro-optic modulator was first studied in our group by Bennett [29]. The design was based on work done by Trutna and Byer [30] in which they used a multiple-pass arrangement to enhance

the gain from a Raman gain cell.

If a ray of light is injected off-axis into a stable optical resonator, it will bounce back and forth between the mirrors. Successive bounces on the mirror surfaces will cause the ray to walk in an oscillatory motion, which is bounded by some maximum excursion from the optical axis and can be contained by sufficiently large mirrors. When the input ray slope and displacement satisfy the proper conditions, it is possible for the rays to trace out circular spot patterns on the mirrors. This is an attractive arrangement for use with the EOM since it allows laser pulses to be injected into the optical resonator and traverse the modulator a specific number of times before they are coupled out.

However, this straightforward principle becomes complicated when a EOM is placed in the optical cavity. The EOM introduces several constraints. First, the optical cavity length is forced to have a discrete set of solutions based on timing conditions resulting from the requirement that optical pulses travel under a cusp (of proper sign) of the electric field. Second, the cross-sectional area of the crystal limits the maximum diameter of the circular path traversed by the light rays. Finally, thermal changes in the crystal cause spatial variations in the refractive index, making it difficult to model.

Timing Requirements

Let us look at the timing requirements in more detail. Recall that a standing wave within an RF resonator can be described as forward and reverse propagating waves and, from Chapter 1, an optical pulse traveling through a resonant EOM will acquire modulation only from the “forward” traveling electric field (i.e., in the direction of pulse travel; Fig. 16). The effect of the reverse traveling wave

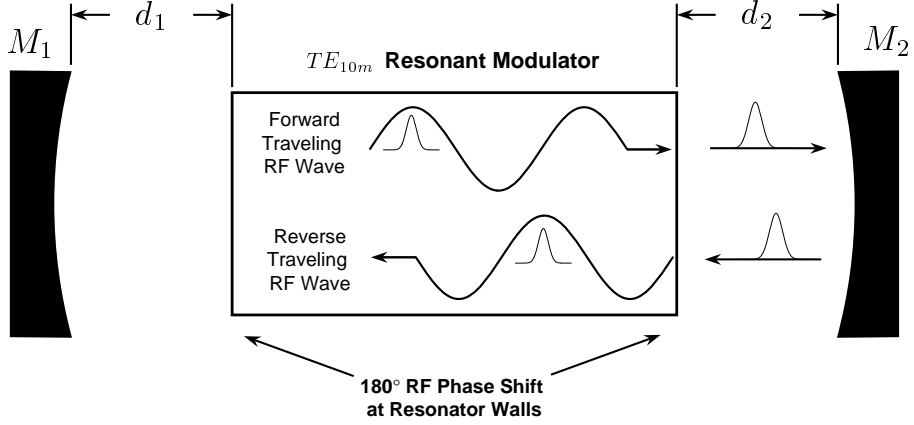


Figure 16. Schematic diagram of a multiple-pass optical cavity showing details important for timing considerations when used with an EOM. The separations d_1 and d_2 should be set such that the optical pulse returns to the modulator under an electric field cusp of the proper sign.

is “washed out.” Also, the positive cusp of a forward wave becomes a negative cusp in the reverse wave due to the 180° phase shift at the resonator walls. Thus, it would be impossible to build a multiple-pass arrangement which had a mirror located *on* one end of the crystal. The quadratic phase which the pulse acquires on the first pass through the EOM would be removed by the second pass since the pulse would be traveling under a cusp of opposite sign. Therefore, the mirrors must have a minimum separation from the closest crystal face. For a TE_{10m} resonator, the single pass optical time delay is $(m + 1)T/2$ and the minimum crystal-mirror separation is given by

$$d_{min} = \frac{1}{2} \left[\left(\frac{m + 1}{2} \right) cT - \ell n_{xtal} \right], \quad (72)$$

where n_{xtal} is the crystal index of refraction and ℓ is the length of the crystal. Any extra length between an end mirror and its closest crystal face must correspond to integer multiples, N , of one-half RF periods. Consequently, the total distance

between a mirror and its corresponding closest crystal face, is

$$d = d_{min} + N\Delta d \quad N = 0, 1, 2, \dots \quad (73)$$

where $\Delta d = cT/2$.

It was stated above that the traveling wave receives a 180° phase shift at each end of the resonator. It should be pointed out that this is only true for “sealed” structures in which the field terminates at a metal wall. The resonator can also be constructed with open ends. In the open-ended configuration the resonator operates slightly above cutoff for the TE_{10m} mode in the dielectric loaded section, and below cutoff in the region without the crystal (at both ends) [31]. Thus, there is an evanescent field extending into the cutoff region which exists to satisfy the boundary conditions at the crystal face. The discontinuity at the boundary causes an extra phase shift which can be very complicated because many cutoff modes are excited to match the fields. However, this is beyond the scope of our analysis and it should suffice to say that if the fields are strongly cutoff, the extra phase shift is quite small.

Ray Path Analysis

We must now determine the mirror curvatures (R_1 and R_2) and separations which will allow us to have the maximum number of passes through the modulator. Before doing this, however, it is customary in resonator theory to define a pair of “resonator g parameters,” g_1 and g_2 . These parameters are

$$g_1 \equiv 1 - \frac{L}{R_1} \quad \text{and} \quad g_2 \equiv 1 - \frac{L}{R_2}. \quad (74)$$

In this case, L is the total *effective* length between the mirrors and is defined as

$$L = d_1 + d_2 + \frac{\ell}{n_{\text{xtal}}}, \quad (75)$$

where d_1 is the distance from M_1 to the nearest crystal face and d_2 is the distance from M_2 to the nearest crystal face. As in gaussian beam propagation calculations (matrix formalism), the crystal length ℓ is divided by the index in order to give the effective length traversed.

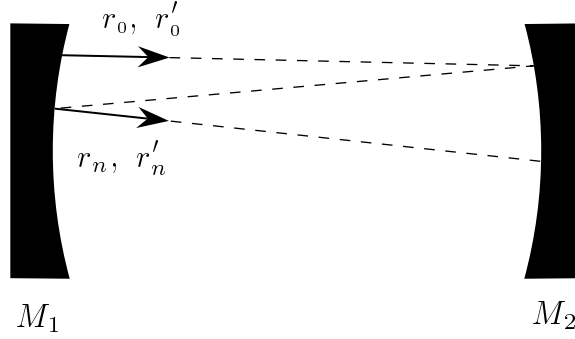


Figure 17. Schematic diagram of an optical cavity showing the ray path conventions for the initial (r_0) and subsequent (r_n) rays.

For this analysis we will be working in the stable resonator regime defined by $0 \leq g_1 g_2 \leq 1$. It is assumed that a ray of light is injected into the resonator and bounces back and forth within the confines of the mirrors (Fig. 17). Let r_0 be the displacement, and r'_0 be the slope of the initial ray. r_n and r'_n are the displacement and slope of the ray at M_1 after n round trips. It can be shown that [32]

$$r_n = r_0 \cos n\theta + \frac{Lg_2}{[g_1g_2(1 - g_1g_2)]^{1/2}} \left(r'_0 - \frac{r_0}{R_1} \right) \sin n\theta \quad (76)$$

where the angle between successive spots (not necessarily adjacent) is given by

$$\theta = \cos^{-1}(2g_1g_2 - 1). \quad (77)$$

This results in a sinusoidal motion across the mirror with an amplitude determined by the initial conditions and an angle determined by the cavity g parameters. This

model can be extended to two dimensions [30]. The x and y coordinates in the plane of M_1 may be expressed as

$$x_n = x_0 \cos n\theta + \frac{Lg_2}{[g_1g_2(1 - g_1g_2)]^{1/2}} \left(x'_0 - \frac{x_0}{R_1} \right) \sin n\theta \quad (78)$$

$$y_n = y_0 \cos n\theta + \frac{Lg_2}{[g_1g_2(1 - g_1g_2)]^{1/2}} \left(y'_0 - \frac{y_0}{R_1} \right) \sin n\theta. \quad (79)$$

In general, these equations define an elliptical path. But, if we let

$$x_0 = \frac{Lg_2}{[g_1g_2(1 - g_1g_2)]^{1/2}} \left(y'_0 - \frac{y_0}{R_1} \right) \quad (80)$$

and

$$y_0 = x'_0 - \frac{x_0}{R_1} = 0, \quad (81)$$

then (78) and (79) reduce to

$$x_n = x_0 \cos n\theta \quad \text{and} \quad y_n = x_0 \cos n\theta, \quad (82)$$

which defines a circular pattern with a radius $r_1 = x_0$ on M_1 and a pattern radius of $r_2 = r_1(g_1/g_2)^{1/2}$ on M_2 . An interesting event occurs when $n\theta = 2\pi k$, where k is an integer. After n round trips, the ray returns exactly to its entrance point (although the slope may be different). This is defined as the “reentrant condition” and allows the ray to be coupled in and out of the cavity with a single mirror or aperture.

Beam Geometry

Since it is the most important aspect of the multiple-pass resonator, we will let the number of transits govern our design. Also, we will assume the initial ray obeys the conditions (80) and (81) in order to form a circular pattern. Since our crystal

is nearly square in cross-section, a circular pattern will be a good fit. Now, suppose the beam is coupled into *and* out of the optical resonator through an aperture in M_1 or, alternatively, with a steering mirror at M_1 . For n round trips between the mirrors, the angle γ between *adjacent* spot centers is

$$\gamma = \frac{2\pi}{n}. \quad (83)$$

Recall that (77) determines the angle between successive bounces and for equally spaced spots θ must be an integer multiple of γ so that $\theta = J\gamma$. Thus, J is the number of times the beam traverses the circular pattern before exiting (or returning to the input spot). The number of unique choices of θ are determined by integer values of J which are not factors* of n in the range

$$1 \leq J \leq \frac{n}{2}. \quad (84)$$

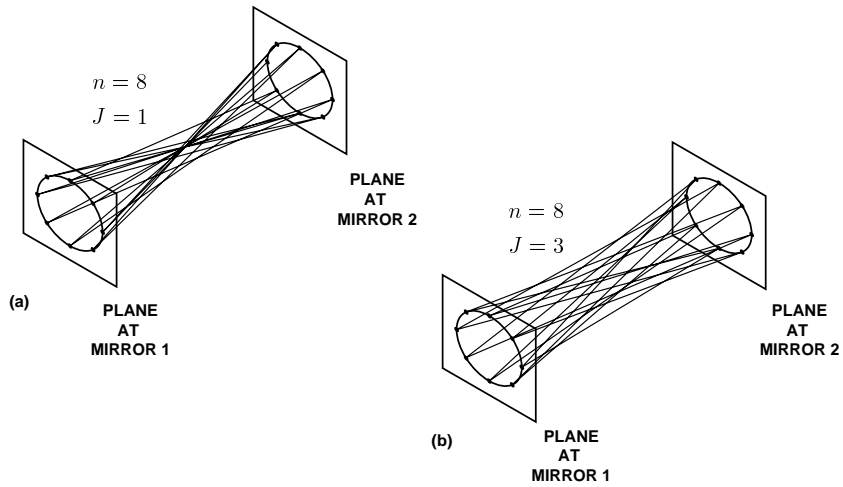


Figure 18. Diagram of an optical cavity showing the ray paths for $n = 8$ round trips and two different step sizes (J). (a) shows a cavity with $J = 1$ and (b) is a cavity with $J = 3$.

* Any value of J which is a factor of n will result in the ray returning to the input point in less than n round trips and exiting the cavity prematurely.

Figure 18 shows an eight spot (round trip) pattern with the two different allowed values of J . Notice how the pattern forms a smaller cross-section at the center for the smaller value of J .

For a symmetric resonator ($g_1 = g_2 = g$), values of g are determined by the set of allowed θ and are defined by

$$g = \pm \left(\frac{\cos(J\gamma) + 1}{2} \right)^{1/2}. \quad (85)$$

Remember, in a symmetrical cavity the beams come to a focus midway between the mirrors and more negative values of g indicate smaller beam waists. If we want to avoid focusing in the modulator, we can use a hemispherical optical cavity. In this case ($R_1 = \infty$, $g_1 = 1$) and values of g_2 are given by

$$g_2 = \frac{\cos(J\gamma) + 1}{2}. \quad (86)$$

Here, smaller g generally implies a greater number of passes and/or more trips around the mirror or cavity. But the g parameter is not arbitrary, since together with L , it will determine the spot size within the cavity. If the beam size becomes too small, it will limit the maximum power by burning the mirrors or crystal and if the beam size becomes too large, the beams may clip within the cavity.

Focusing Properties

Since it is undesirable to focus the beam inside the crystal (possible laser damage), we chose a hemispherical cavity as the optical resonator. Therefore, throughout the rest of this analysis we will only discuss the hemispherical configuration. As stated earlier, crystal size is the major restriction on the number of passes through the EOM. To prevent the beams from clipping at the crystal face we will add one

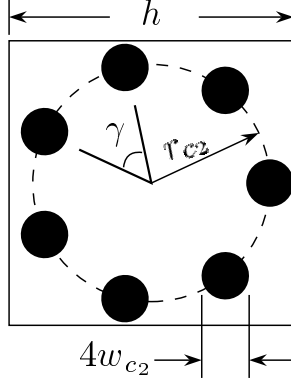


Figure 19. Representation of a sample spot pattern on the crystal face nearest M_2 . The spots are depicted as four times their gaussian radius w_{c_2} in diameter and lie on a circle with a radius r_{c_2} . The smallest crystal cross-sectional dimension is labeled as h .

more constraint. We assume that the maximum pattern radius at the crystal face nearest M_2 is $r_{c_2} = h/2 - 2w_{c_2}$, where h is the smallest cross-sectional dimension of the crystal and w_{c_2} is the beam radius at the crystal face (see Fig. 19). Assuming a constant angular separation γ , the larger r_{c_2} , the greater the number of passes we can obtain. From the equation for r_{c_2} above, we can see it is greatest when w_{c_2} is at a minimum. Using gaussian beam propagation theory, w_{c_2} is related to the beam waist w_0 at M_1 by

$$w_{c_2} = w_0 + \frac{\lambda}{\pi w_0} \left(d_1 + \frac{\ell}{n_{\text{xtal}}} \right). \quad (87)$$

The ideal beam waist can be determined by using (87), taking the derivative with respect to w_0 , setting it equal to zero, and solving for w_0 . This yields

$$w_0 = \sqrt{\frac{\lambda}{\pi} \left(d_1 + \frac{\ell}{n_{\text{xtal}}} \right)}. \quad (88)$$

Notice that d_1 should be small to keep the beam waist, and therefore w_{c_2} , at a minimum.

Now we need to know what the launching conditions are for a hemispherical cavity when the steering mirror is at M_1 . From Eq.'s (80) and (81), $x'_0 = y_0 = 0$, this leaves only x_0 and y'_0 to be determined. Using Snell's Law and some trigonometry we can show

$$r_{c_2}^2 = x_0^2 + \left[y'_0 \left(d_1 + \frac{\ell}{n_{\text{xtal}}} \right) \right]^2. \quad (89)$$

Employing (80) and (81) with $R_1 = \infty$ and solving for y'_0 yields

$$y'_0 = \frac{x_0 \sqrt{g_2(1-g_2)}}{Lg_2}. \quad (90)$$

Substituting this into (89) and solving for x_0 produces

$$x_0 = \frac{r_{c_2}}{\sqrt{1 + \frac{1-g_2}{L^2 g_2} \left(d_1 + \frac{\ell}{n_{\text{xtal}}} \right)^2}}. \quad (91)$$

There is one final consideration. If the spots at the injection point on M_1 are not well separated, it will be very difficult and expensive to insert a steering mirror or aperture which does not interfere with the paths of the other rays. If the rays are occluded in any manner, they will scatter and cause diffraction fringes, severely reducing the throughput efficiency. However, even if the spots at the input are well separated, the input beam must be mode matched to the cavity. If it is not, the beam will “scallop” or undulate while traversing the cavity, possibly clipping the crystal or steering mirror.

3.4 Experimental Results of an Active Pulse Compressor

In order to demonstrate a practical active compression system we constructed a 14-pass optical cavity around the EOM described in Chapter 2. Many different configurations were analyzed, but only one was a good compromise between trying

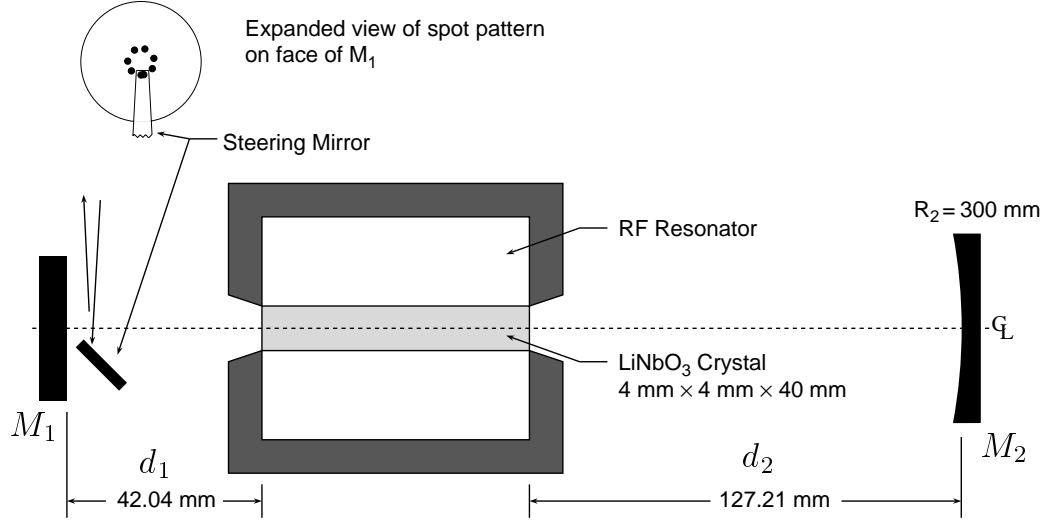


Figure 20. Hemispherical fourteen-pass optical cavity used in active compression experiment. The beam is coupled into and out of the cavity via the steering mirror at M_1 .

to achieve a large number of passes through the EOM and overall functionality. A drawing of the final arrangement is shown in Fig. 20. The mirror separations d_1 and d_2 were set at d_{min} and $d_{min} + 2\Delta d$, respectively. This allowed a seven round trip pattern ($J = 2$) which had a spot separation large enough to insert the specially cut steering mirror (see expanded view in Fig. 20). Notice the pattern was not radially symmetric because M_2 had a 300 mm radius of curvature, instead of 307 mm as established when using the theoretical analysis of the previous section.

A summary of the data concerning the hemispherical optical cavity is shown in Table 3. Since a readily available mirror radius was used for M_2 , the values for the step and separation angles vary slightly from the theoretical numbers generated from the analysis in the previous section. In fact, as pointed out earlier, the pattern no longer has a constant angle of separation (γ). Also, the step angle (θ) is such that the input and output spots are 8° apart at M_1 . This results in an input/output spot center separation of $\sim 300 \mu\text{m}$. Thus, the steering mirror had to be large enough to

Variable	Value	Variable	Value (mm)	Variable	Value (mm)
n	7	R_1	∞	w_2	0.4665
J	2	R_2	300	w_{c_2}	0.2403
β	$\sim 50^\circ$	d_1	42.05	$r_1 = x_0$	1.4022
θ	104.6°	d_2	127.21	r_2	2.2929
g_1	1	L	187.81	r_{c_2}	1.5120
g_2	0.374	$w_1 = w_0$	0.2217	y'_0	0.5534°

Table 3. Parameter values used in the experimental fourteen-pass optical cavity.

contain both spots. A standard ray matrix approach similar to Siegman’s periodic structure analysis [8] was used to verify the location of each of the spots at the mirrors.

The experimental setup used with our multiple-pass resonant modulator (time lens) is the same as the one shown in Fig. 13. The 85 ps mode-locked pulses originated from a Coherent Antares Nd:YAG laser operating at an 80 MHz repetition rate. The 1.76 GHz signal used to drive the time lens was synthesized from the same 10 MHz source used to create the 40 MHz modelocker drive signal. This insured that the laser pulses were phaselocked to the RF signal driving the time lens. The RF delay line was adjusted so that the pulses acquired positive frequency chirp when passed through the lens. To verify that the pulses were under a cusp, the pulse’s spectrum was monitored with a 3/4-meter spectrometer as the delay line was adjusted (Fig. 22). When the RF power to the time lens was turned on and off, the peak of the spectrum did not shift indicating a lack of linear phase. This lack of phase shift, in addition to watching for a minimum pulse width after the gratings, insured the pulses were under the proper region of the RF field.

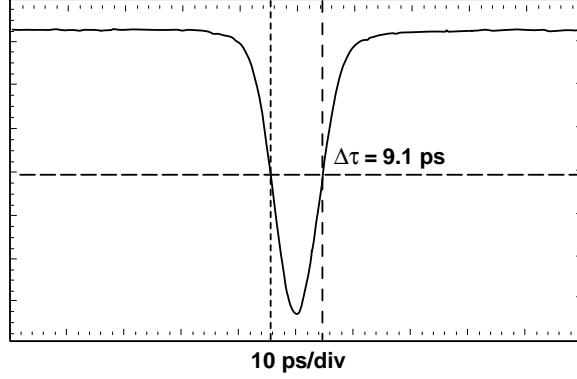


Figure 21. Autocorrelation trace of a pulse compressed with the active pulse compression setup shown in Figs. 13 and 20. Notice the complete absence of a pedestal or wings indicating nearly uniform linear chirp.

When testing the active compression system, 32 Watts was the maximum RF power I could use with the time lens before electric field breakdown occurred between the electric field probe and resonator. With the gratings adjusted for a minimum pulse width at the maximum RF power, the intensity autocorrelation function had a width of 9.1 ps. If a sech^2 pulse shape is assumed, the pulse width deconvolves to 5.9 ps. This is a compression ratio of 14.4:1 when compared to the input pulse width of 85 ps. The autocorrelation function of a typical output pulse, taken without averaging, is shown in Fig. 21. The time lens had a throughput efficiency of 50% and the double-pass grating pair had a throughput efficiency of 63%, for a total system efficiency of 32%. This resulted in a 4.6:1 increase in peak power (14.4×0.32). The time lens throughput efficiency was much lower than the expected 85% (based on surface reflection losses). This was due in part to poor modematching of the input beam to the multiple-pass optical cavity and thermal index changes of the LiNbO_3 crystal.

As Fig. 21 shows, the actively compressed pulses are free from any pedestal or wings typical of fiber-grating compression. Also apparent is the lack of relative

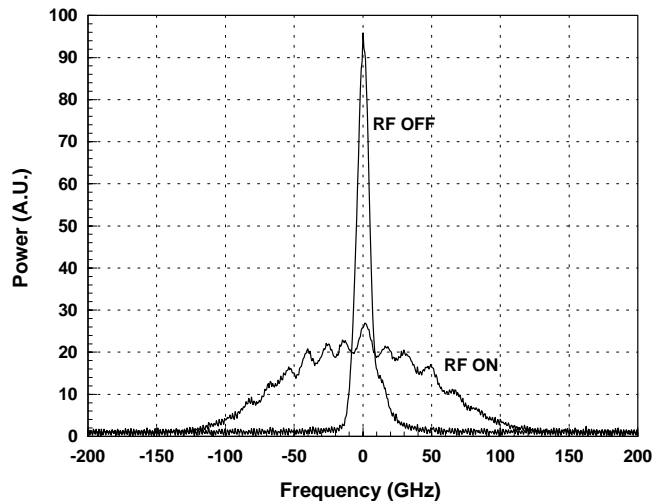


Figure 22. Spectrum of an actively compressed pulse for a RF drive power of 0 and 32 Watts. The ‘RF off’ spectrum has a width of 9 GHz (FWHM) and the ‘RF on’ spectrum has a width of 110 GHz.

amplitude noise even though the averaging was turned off. In fact, the amplitude noise is the same as that of the input pulse ($< 2\%$ rms).

As stated earlier, the spectrum of the pulse is a very good diagnostic of the operation of the time lens. Figure 22 shows the pulse spectrum with maximum RF power applied to the time lens and with no RF power. The chirped spectrum has a width of ~ 110 GHz. This results in a time-bandwidth product of 0.65 ($5.9 \text{ ps} \times 110 \text{ GHz}$), twice the transform limit for a sech^2 pulse. The unchirped spectrum has a width of ~ 9 GHz. A time-bandwidth product of 0.76 indicates the presence of chirp in the laser pulse. To determine if any of that chirp was linear, we passed the laser pulses through a diffraction grating pair and were able to compress the pulses to 69 ps. This results in a time-bandwidth product of 0.62, about twice the transform limit.

3.5 Future Investigation

The next logical step in pulse compression systems would be the design and

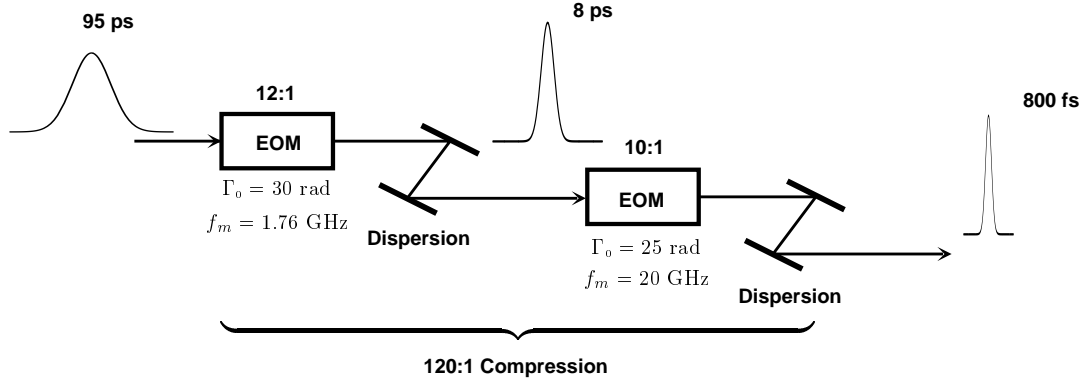


Figure 23. Active compression using a compound time lens system. The first stage provides a compression ratio of 12:1, the second a ratio of 10:1, for a total compression of 120:1.

implementation of a compound time lens system. This would allow very large compression ratios while keeping the demands on a single lens reasonable. For example, Fig. 23 shows how a compression system with a final compression ratio of 120:1 could be realized. The peak phase deviation for each time lens is below 30 rad. To do this in a single stage at 1.76 GHz would require the lens to have 300 rad of peak phase deviation!

One of the drawbacks to a compound system is the possibly low throughput efficiency. The system discussed in this chapter had a system efficiency of 32%. If we assume about the same efficiency for both stages of a compound system, we obtain a total system efficiency of 10% and a 12:1 increase in peak power. Therefore, in the future it will be important to develop time lenses which operate at higher frequencies for use in the second stage and also improve the system efficiencies of each lens.

Active Additive Pulse Modelocking

4

To date, the technique of additive pulse modelocking (APM) has relied on an external cavity with a nonlinear passive element [33]. Usually, this consists of a length of optical fiber which generates additional frequency components in the external cavity. Traditional APM suffers from several drawbacks. These include, fiber coupling losses, inconvenience in changing fiber lengths, sensitivity to environmental fluctuations, and the intimate relationship between the power in the external cavity and the generated frequency spectrum. These characteristics result in a substantial sacrifice of available average laser power [34] and a limited range of useful pulse widths [35]. To overcome the limitations of the passive approach, we explored a technique that incorporates an electro-optic modulator as an active element in the external cavity. Although this modulator is the same one used as a time lens described in earlier chapters, temporal imaging does not play a role in this case. The principal advantage of this approach is that it allows for independent control of the amount and type of phase modulation irrespective of the optical power in the external cavity. Therefore, it has been designated *active additive pulse modelocking* (AAPM). In addition, the bulk optics comprising the cavity result in greater coupling efficiency when compared to a single mode fiber.

4.1 Additive Pulse Modelocking

Figure 24 shows a standard APM experimental setup. The main laser cavity can be almost any type of mode locked laser. Nd:YAG, Nd:YLF, Ti:Sapphire, and color center lasers, both passively and actively mode locked, have all been used in APM systems [34–36]. The key is the nonlinearity in the external cavity. Recall that a mode locked pulse train results when the longitudinal modes of the laser cavity have some coherent phase relationship with one another. In the simplest case, all modes have the same phase. This occurs only if there is some coupling between the modes. This mode coupling can be induced using many different techniques such as loss modulation, frequency modulation, or synchronous pumping. Passive methods, like intracavity saturable absorbers, can also provide the mode coupling. This begs the question, why not place the nonlinear element in the main cavity? Although a nonlinear element can be used in the main cavity to enhance modelocking, this would also significantly increase the lasing threshold. On the other hand, if the nonlinear element is placed in an external cavity, the mode coupling may be accomplished without a corresponding increase in lasing threshold.

The frequency domain view of APM is not the only way to look at the process. Ippen and Haus treat the phenomenon in the time domain [37] and this shows the origin of the designation “additive pulse modelocking”. Again, using Fig. 24 as a reference, consider a mode locked laser with part of its output passed through a short length of optical fiber before being reinjected into the main cavity. The path length of the external cavity is an integer multiple of the main cavity’s, so that the reinjected pulse interferes coherently with the main cavity pulse. Usually, a piezoelectric stack is used to control the external cavity length and thereby maintain

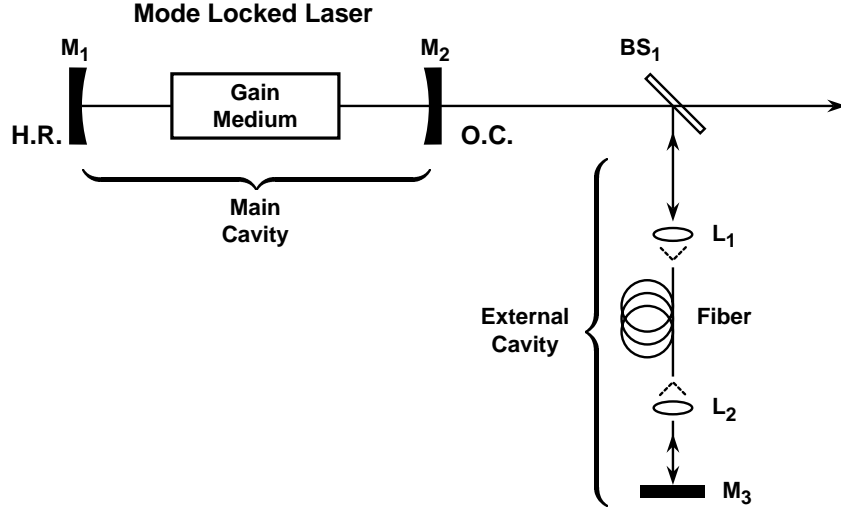


Figure 24. Schematic diagram of a typical APM configuration. The main cavity can be almost any type of passively or actively mode locked laser. HR, high reflecting; OC, output coupler; BS, beam splitter; L, coupling lens.

the phase of the interference.

To illustrate, consider the case in which the fiber does not disperse the pulse (i.e., the main cavity pulse has the same shape as the reinjected pulse). Also, assume that even without the nonlinearity the phase of the reinjected pulse leads that of the main cavity pulse by some angle between 0 and π . Thus, the interference of the two pulses can be partially destructive. If there is any self-phase modulation in the external cavity, then the interference will be more additive near the peak of the pulse than in the wings. The net effect is that the laser cavity sees the external cavity as a termination which returns a shorter pulse than is injected. Since this occurs as a result of the pulses from the main cavity and external cavity interfering additively at the output coupler, the process is called additive pulse modelocking. It should be noted that this occurs without any pulse reshaping in the external cavity. In fact, it turns out that the process is quite unresponsive to changes in the pulse shape.

4.2 Active Nonlinear Element

Using a passive nonlinear element in the external cavity imposes restrictions on the areas of operation for the system since the amount of nonlinear phase retardation imparted to the external cavity pulse is dependent on the power in that cavity. The addition of loss elements to the external cavity can give some flexibility but this reduces the efficiency and maximum available power. In the case of a fiber as the nonlinear element, the length can be changed to vary the amount of SPM experienced by the pulse. Unfortunately, this can be a time consuming and difficult procedure. By using an electro-optic modulator as the nonlinear element, we uncouple the external cavity's phase-power dependence. In fact, we gain considerable control over the amount and *type* of phase modulation. By using a delay line to change the phase of the RF drive we can move through the sinusoid, progressing from linear phase at the nodes to quadratic phase at the cusps. This allows for a more thorough investigation of the relationship between the influence of the external cavity on the main cavity.

Experimental Configuration

Figure 25 shows the experimental configuration of our active APM system. The external cavity is designed to have the same round trip time as the main laser cavity (12.5 ns) with the beam making a double pass through the resonant electro-optic modulator. The EOM is driven at 1.76 GHz or the 22nd harmonic of the 80 MHz laser repetition rate. It is also positioned 1.5 RF periods from M_1 . This is to satisfy the timing requirements as outlined in Section 3.3. Microwave power is supplied to the modulator from a synthesizer and amplifier which are phaselocked to the laser modelocker through the lab's primary frequency standard (10 MHz). The round

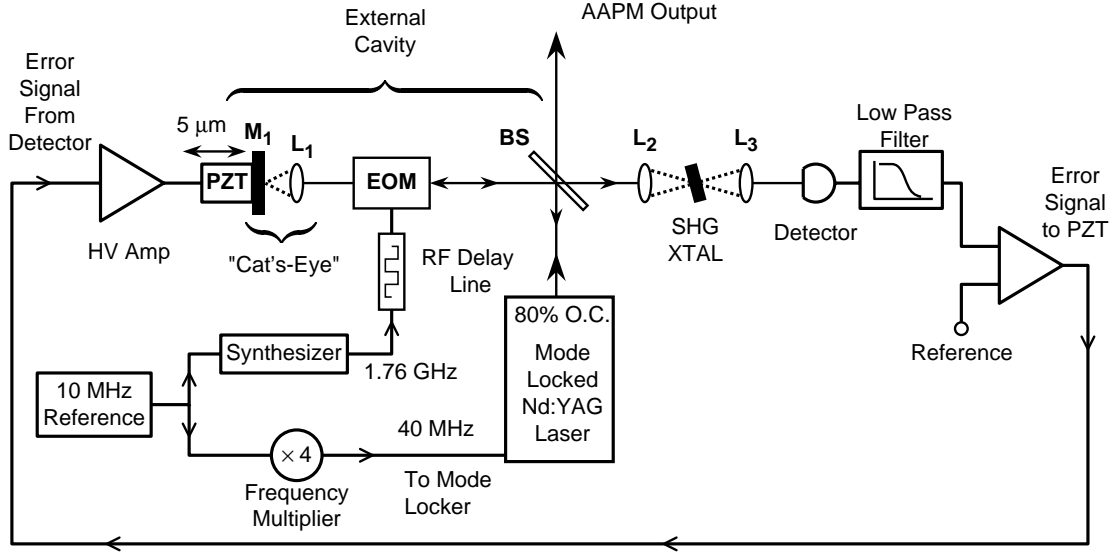


Figure 25. Schematic diagram of the AAPM configuration. The laser is an AM mode-locked Nd:YAG producing 85 ps pulses at an 80 MHz repetition rate. EOM, electro-optic modulator; PZT, piezo electric translator; BS, beam splitter; L, focusing lens; O.C., output coupler.

trip loss in the external cavity is less than 2 percent.

Mode-matching of the external cavity beam to the main cavity is accomplished through a “cat’s-eye” configuration at M_1 [38]. It consists of mirror M_1 at the focus of a short (52 mm) focal length lens L_1 . Since the radius of curvature at the waist (focus) of the gaussian beam is infinite, it is conveniently matched to the flat high reflector. In the absence of aberrations, the mode matching is perfect. However, there are two other considerations. First, the spot size must be sufficiently large to avoid burning the HR coating. Second, the Rayleigh range at the focus must be significantly larger than the expected movement of the PZT (typically $< 25 \mu\text{m}$). Otherwise, the mode-matching will vary with the external cavity length as the PZT is adjusted to match the external cavity to the main cavity.

The strength of coupling between the two cavities depends on several factors. The reflectivity of the output coupler in combination with the beam splitter re-

flectivity determines the maximum amount of coupling. The quality of the mode match can then be used to reduce the coupling strength. But, this is less efficient than changing the beam splitter reflectivity since energy not reinjected back to the cavity is wasted.

External Cavity Stabilization

Since the phase between the external cavity pulse and the main cavity pulse is critical for APM operation, the external cavity length must keep a fixed relationship with the main cavity. To accomplish this, I used an active stabilization scheme with the external cavity. The active stabilization scheme was based on work done by Mitschke and Mollenauer to stabilize their soliton laser [38]. However it was necessary to include a second harmonic generation (SHG) crystal to increase the sensitivity of the feedback. Unlike the soliton laser, the time averaged output power of our laser did not vary significantly as the external cavity mirror was translated. But, the peak power of the pulses, as well as the pulse width, was very sensitive to the mirror motion. This indicated that the peak pulse power in the external cavity (also the main cavity) varied with ϕ , the round trip optical phase shift in the external cavity, similar to what is shown in Fig. 26. Also, the most stable point of operation was slightly below the point of maximum peak power. Thus, at least in the region around stable operation, the peak power in the external cavity is a good indication of ϕ .

The key is maintaining ϕ at ϕ_{stable} is by converting the peak power of the pulse into a time averaged power which can be monitored with a simple detector. This is accomplished with a SHG crystal. The residual power from the external cavity which is not reinjected into the main cavity is focused into the crystal, generating a

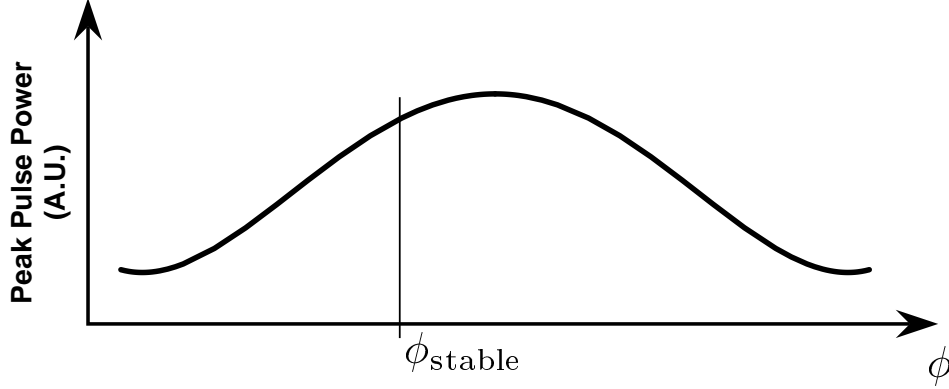


Figure 26. Deviation of external cavity peak pulse power with round trip optical phase shift ϕ .

second harmonic signal (Fig. 25). This signal varies as the square of the fundamental's peak power, making it very sensitive to changes in the peak. With this in mind, the circuitry shown in Fig. 25 is now easily understood. The output of the detector is a measure of the average second harmonic power generated, and hence the peak power in the external cavity. The error signal for control of ϕ is then generated by taking the difference between the detector signal and an empirically set reference voltage. The low pass filter is used to keep the error signal's bandwidth below that of the PZT's resonance (~ 5 KHz). The high voltage opamp boosts the error signal and drives the PZT attached to the end mirror M_1 . Assuming the signal polarities are correct, the circuit forms a closed negative feedback loop. Thus, a deviation in ϕ produces a change in the detector signal that results in a corrective displacement of M_1 .

Figure 27 shows a plot of the AAPM's output intensity noise simultaneously with the error signal which drives the PZT while the stabilization circuit was enabled. Data was taken for several RF drive powers but in this case the RF power was 26 Watts to highlight the laser noise. The intensity noise could be as low as

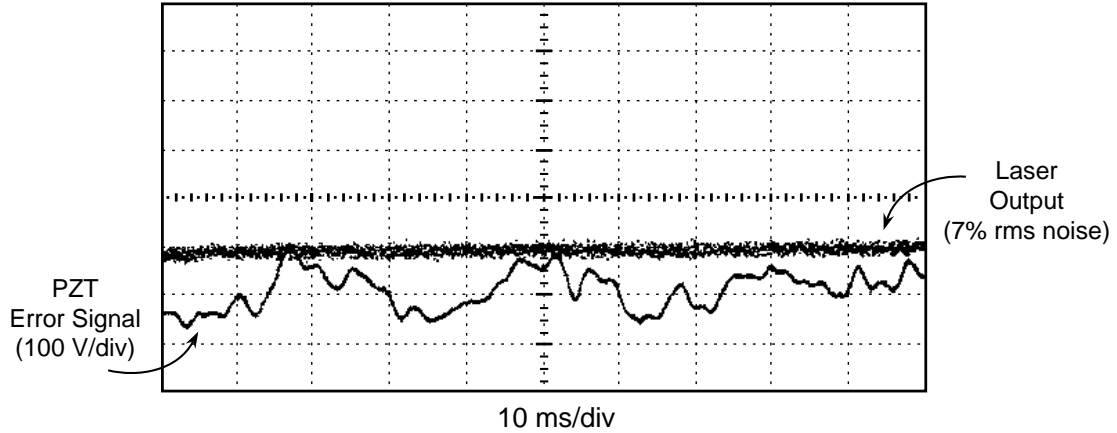


Figure 27. Oscilloscope plots showing the intensity fluctuations (noise) at the laser output and the error signal which drives the PZT. The PZT has a response of 500 nm/100 V.

4% rms just above the shortest pulse widths when the stabilization was enabled. Compared to greater than 25% without the stabilization. Note the PZT would tend to fluctuate around center values which were approximately 1 μm apart. This is as expected since the Nd:YAG wavelength is 1.06 μm and the external cavity would have to jump from one longitudinal mode to the next when trying to match with the main cavity. The bandwidth of the stabilization circuit was set to 750 Hz at the -3 dB point. The lowpass filter had a rolloff of 40 dB/decade with an additional notch filter at 80 kHz to suppress the strong relaxation oscillations of the laser. Once the setup was complete, stable operation could be maintained for about an hour before a large perturbation or thermal change would cause a jump in the output.

4.3 Some Experimental Results

To demonstrate the AAPM system, the configuration shown in Fig. 25 was used with beam splitter values of 5%, 10%, and 30%. The best results were obtained with the 10% beam splitter. Figures 28 and 29 show typical output pulses from

the AAPM system with 7 Watts of RF power driving the EOM. Figure 28 is an autocorrelation trace with a 31.5 ps width. If a sech^2 pulse shape is assumed, this deconvolves to 20.4 ps. Figure 29 is the same pulse observed with a fast photodetector (18 ps response). It has a measured width of 26 ps which indicates approximately a 19 ps incident pulse when the detector response is deconvolved. Note the ringing after the pulse is due to the detector response.

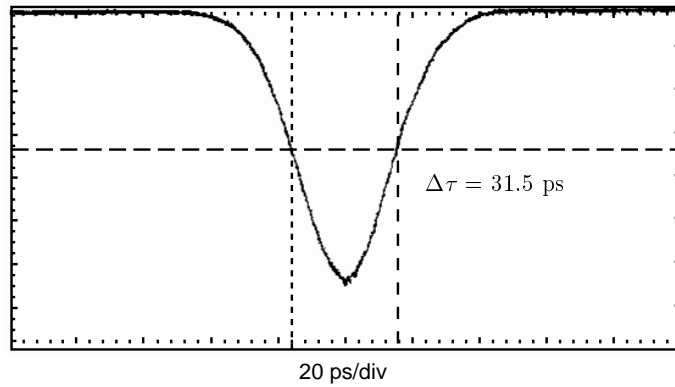


Figure 28. A typical autocorrelation trace of the laser output pulses. The EOM RF drive power was 7 Watts.

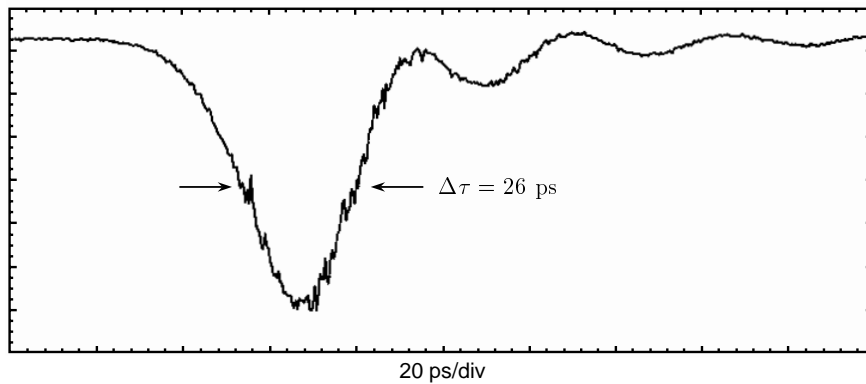


Figure 29. A typical AAPM output pulse measured on a fast photodetector (18 ps response). The EOM RF drive power was 7 Watts and the averaging was set at 8.

To compare the operation of the AAPM system with both the 5% and 10% beam splitters, the pulse width and spectrum were measured as a function of applied

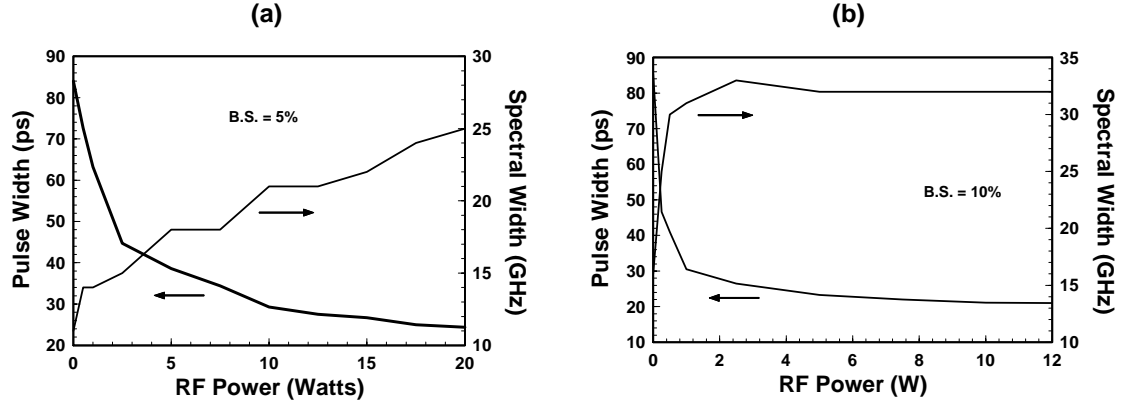


Figure 30. AAPM pulse characteristics as a function of RF drive power and beam splitter mirror percentage. (a) beam splitter is 5%; (b) beam splitter is 10%.

RF power (see Fig. 30). Data was not taken with the 30% beam splitter since it resulted in extremely noisy output which could not be suppressed below 20% rms even with the stabilizer operating. As Fig. 30 shows the slopes for the 10% beam splitter are steeper than for the 5% beam splitter. This is expected since the increased beam splitter reflectivity strengthens the coupling between the two cavities thereby enhancing the mode coupling (locking) in the main cavity for a given amount of phase modulation from the EOM. The spectrum increased almost linearly with RF power for the 5% beam splitter while the 10% beam splitter spectrum increased very steeply at first and then leveled off. Neither of these correlated with their respective pulse width plots, indicating a large variation in the time-bandwidth product of the AAPM pulses as the RF power was changed. However, it was not possible to verify if there was any linear chirp present in the pulses.

In addition to the desired stable modes of operation, it was observed that the laser would occasionally run in an astable mode in which the laser switches back and forth at frequencies from hundreds to thousands of hertz between two distinctly different pulse modes. On the autocorrelation display, which is scanned at 15 Hz,

this astable mode shows up as two overlapping traces with a $\sim 2:1$ pulse-width ratio (see Fig. 31). This type of operation was also noticed in the soliton laser developed by Mollenauer, et al. [38].

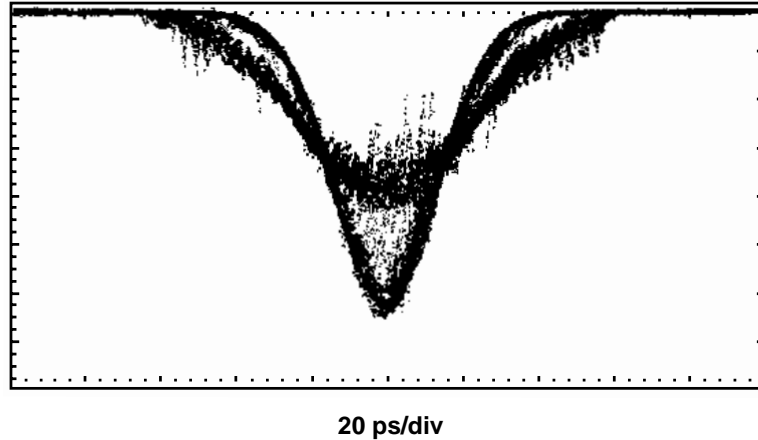


Figure 31. Autocorrelation trace showing dual pulse traces indication an astable mode of operation for the AAPM system. The autocorrelation pulse widths are approximately 32 ps and 60 ps.

As mentioned at the beginning of this chapter, the use of bulk optics in the external cavity results in a very high efficiency. The average output power available with the 5% beam splitter was 23.7 Watts and with the 10% beam splitter the average power was 21.5 Watts from an original 24 Watts (no external cavity). Thus, we gained a factor of four decrease in pulse width with only a 10% decrease in available power! However, this gain currently comes with a noise penalty. The original laser noise before the addition of the external cavity was less than 1% rms. Even when operating at its best, the AAPM laser still produced 4% rms noise. This is unacceptable for most applications, especially when the current cost of the modulator (RF source, crystal, etc.) is included.

Some interesting questions arose out of this experiment; how were the pulses being modulated (linear, quadratic, etc.) and how did this influence the system

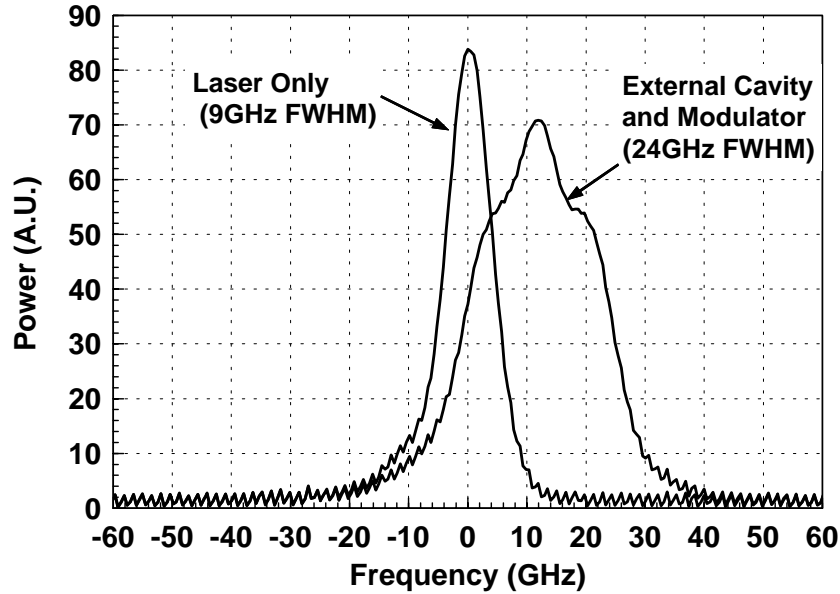


Figure 32. A typical AAPM spectrum plot showing a shifted chirped pulse. RF drive, 15 Watts; beamsplitter, 5%.

performance? The spectrum plots indicate that the pulses were experiencing a combination of linear and higher order phase modulation when producing the shortest pulses (Fig. 32). This can be explained in the following manner; if the AAPM spectrum isn't shifted from the laser spectrum then the pulses must be centered under a cusp (quadratic phase). If the AAPM spectrum has the maximum frequency shift possible, then the pulses must be at a node of the electric field (linear phase). At any other point in the field, the pulses will receive some phase modulation which is a combination of linear and higher order terms. Yet, stable operation could be obtained with many different settings of the RF phase (delay line) by merely making slight adjustments to the external cavity length. For instance, every 85° change in the RF phase required a cavity length change of 400–900 μm . This corresponds to a change in round trip delay of 2.5–6 ps. Although the resulting output pulses were not necessarily the shortest, the output was stable.

4.4 Future Investigation

In conclusion, this beginning work in AAPM has opened up an area of investigation rich with opportunities to further develop the theory underlying APM. The significant advantages offered by this new approach to APM in independently controlling the experimental parameters will also allow a more complete understanding and verification of existing and future work in additive pulse modelocking. Finally, the application of this technique to other (older) laser systems may breath new life into what was a waning technology. The key will be to develop a complete theoretical model which will allow the optimum point of operation to be discerned.

The ability to impart an arbitrary amount of quadratic phase modulation will extend many current technologies in the optical sciences. Applications such as temporal microscopy (waveform expansion) or waveform compression for coherent spectroscopy (i.e., preparing waveforms on a large time scale and then compressing) have been discussed. But, indirect uses, like active additive pulse modelocking, are possible only because of the relatively large phase modulations afforded by resonant electro-optic time lenses.

This thesis has presented preliminary work which was done to address the technological hurdles associated with implementing practical time lenses. Although resonant electro-optic structures provide greater phase modulation than previously attained, current time lenses are still quite weak when compared to their spatial counterparts. Most of the lenses used to collect and convey spatial information have f -numbers ranging from $f/1$ – $f/20$. In contrast, the time lens discussed in earlier chapters has a temporal f -number $f_T^\# = 3,200$ and a corresponding resolution of 11 ps. This is equivalent to a 1'' diameter lens with a focal length of 81 m. There are few practical applications where such a weak time lens might be useful. Active pulse compression is one. Yet, to achieve a more reasonable $f_T^\#$ (say, $f_T^\# = 10$) we would need a peak phase deviation of 600 rad at a modulation frequency of 50 GHz.

This would yield a temporal resolution of 33 fs @ 1 μm (i.e., 10 times the carrier period) and a temporal aperture of 3.3 ps.

If we wanted to use such a lens for a time microscope with a magnification of 300, it would allow a fast detector-oscilloscope combination (10 ps response) to directly measure optical waveforms with a resolution of 33 fs. Now, the required input and output dispersions for such a system are approximately 0.017 fs/GHz and 5 fs/GHz respectively. Thus, the input could be 1 m of fused-silica fiber and the output a pair of gratings (or 300 m of fiber). The only other requirement is a *true* temporal aperture of 3.3 ps.*

The future will undoubtedly see many more benefits from the development of temporal imaging in general and time lenses in particular. These benefits will enrich not only the optical sciences, but many others as well.

* 'True' indicates an aperture which will only allow 3.3 ps of the dispersed input waveform through the lens to avoid overfilling its usable aperture of $T/6$.

This appendix shows the development of an expression for the maximum compression ratio of a gaussian pulse after it has passed through an active compression system [39].

Consider an arbitrary input pulse with an envelope function $A(0, \tau)$ incident on a electro-optic time lens with a transfer function $H(\tau)$.

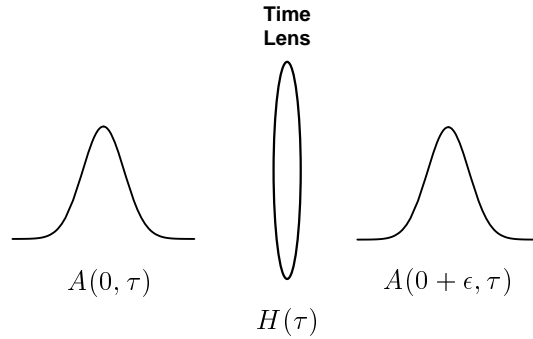


Figure 33. Arbitrary input pulse before ($A(0, \tau)$) and immediately after ($A(0 + \epsilon, \tau)$) a time lens ($H(\tau)$).

From Eq. (A40) we know

$$\begin{aligned} H(\tau) &= \exp \left[i \frac{\Gamma_0 \omega_m \tau^2}{2} \right] \\ &= \exp \left[i \frac{\tau^2}{4\beta} \right], \quad \beta = \frac{1}{2\Gamma_0 \omega_m} \end{aligned} \quad (\text{A1})$$

where Γ_0 is the peak phase deviation and ω_m is the angular microwave frequency of the EOM. Immediately past the time lens ($\xi = 0 + \epsilon$) we have

$$A(0 + \epsilon, \tau) = A(0, \tau)H(\tau). \quad (\text{A2})$$

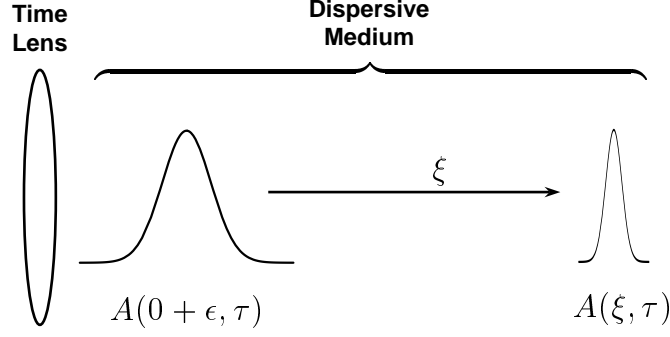


Figure 34. Chirped input pulse before ($A(0 + \epsilon, \tau)$) and after ($A(\xi, \tau)$) propagating a distance ξ through a dispersive medium.

Let the pulse propagate through a dispersive medium a distance ξ . This introduces a quadratic phase in the frequency domain,

$$\begin{aligned} \mathcal{G}(\omega) &= \exp \left[-i \frac{\xi}{2} \frac{d^2 \beta}{d\omega^2} \omega^2 \right] \\ &= \exp [-i\alpha\omega^2] \quad \alpha = \frac{\xi}{2} \frac{d^2 \beta}{d\omega^2} \omega^2. \end{aligned} \quad (\text{A3})$$

If $\mathcal{A}(\xi, \omega) = \mathcal{F}\{A(\xi, \tau)\}$, then

$$\mathcal{A}(\xi, \omega) = \mathcal{F}\{A(0, \tau)H(\tau)\} \cdot \mathcal{G}(\omega). \quad (\text{A4})$$

Inverse Fourier transforming $\mathcal{A}(\xi, \omega)$ back to real space yields

$$A(\xi, \tau) = \mathcal{F}^{-1}\{\mathcal{A}(\xi, \omega)\} = \frac{1}{2\pi} [A(0, \tau)H(\tau)] * [G(\tau)], \quad (\text{A5})$$

where

$$G(\tau) = \mathcal{F}^{-1}\{\mathcal{G}(\omega)\} = \frac{1}{2\pi} \left(\sqrt{\frac{1}{i4\pi\alpha}} \exp \left[i \frac{\tau^2}{4\alpha} \right] \right). \quad (\text{A6})$$

Expanding the convolution gives

$$A(\xi, \tau) = \frac{1}{4\sqrt{i\pi^3\alpha}} \int_{-\infty}^{\infty} A(0, \tau')H(\tau') \exp \left[i \frac{(\tau - \tau')^2}{4\alpha} \right] d\tau'. \quad (\text{A7})$$

Substituting (A1) for the lens function $H(\tau')$ yields

$$A(\xi, \tau) = \frac{\exp\left[i\frac{\tau^2}{\alpha'}\right]}{2\sqrt{i\pi^3\alpha'}} \int_{-\infty}^{\infty} A(0, \tau') \exp\left[i\tau'^2 \left(\frac{1}{\alpha'} + \frac{1}{\beta'}\right)\right] \exp\left[i\frac{2\tau\tau'}{\alpha'}\right] d\tau', \quad (\text{A8})$$

where $\alpha' = 4\alpha$ and $\beta' = 4\beta$. This is the general solution for the effect of a time lens and subsequent propagation in a dispersive medium, on an optical pulse with an initial field envelope $A(0, \tau)$.

We now look at the specific case where we have a complex gaussian pulse shape as the initial pulse, i.e.,

$$A(0, \tau) = \exp[-\Gamma\tau^2] \quad \begin{array}{l} \Gamma = a - ib \quad \dots \text{gaussian pulse parameter} \\ a = \frac{2 \ln 2}{\tau_p^2} \quad \dots \tau_p = \text{intensity pulse width (FWHM)} \\ b = \frac{1}{2} \frac{d\omega}{dt} \quad \dots \text{chirp parameter} \end{array}$$

If the pulse does not have any chirp initially then $b = 0$ and

$$A(0, \tau) = \exp[-a\tau^2]. \quad (\text{A9})$$

Substituting this into the general solution (A8) yields

$$A(\xi, \tau) = \frac{\exp\left[i\frac{\tau^2}{\alpha'}\right]}{2\sqrt{i\pi^3\alpha'}} \int_{-\infty}^{\infty} \exp\left[i\left(\left[\frac{1}{\alpha'} + \frac{1}{\beta'}\right] + ia\right)\tau'^2\right] \exp\left[i\frac{2\tau\tau'}{\alpha'}\right] d\tau'. \quad (\text{A10})$$

This is a Fourier transform of a complex gaussian and after simplification we get

$$A(\xi, \tau) = \frac{1}{2\pi\sqrt{\alpha' \left(\left[\frac{1}{\alpha'} + \frac{1}{\beta'}\right] + ia\right)}} \times \exp\left[i\left(\frac{1}{\alpha'} - \frac{1}{\alpha'^2 \left(\left[\frac{1}{\alpha'} + \frac{1}{\beta'}\right] + ia\right)}\right)\tau^2\right]. \quad (\text{A11})$$

Now, consider only the argument of the exponential and manipulate it to fit the form of $\Gamma = a' - ib'$.

$$A(\xi, \tau) = \underbrace{\frac{-a}{\alpha'^2 \left[\left(\frac{1}{\alpha'} + \frac{1}{\beta'} \right)^2 + a^2 \right]}}_{a'} - i \underbrace{\left[\frac{\left(\frac{1}{\alpha'} + \frac{1}{\beta'} \right) - \alpha' \left(\left[\frac{1}{\alpha'} + \frac{1}{\beta'} \right]^2 + a^2 \right)}{\alpha'^2 \left(\left[\frac{1}{\alpha'} + \frac{1}{\beta'} \right]^2 + a^2 \right)} \right]}_{b'} \quad (\text{A12})$$

Since the real part (a') controls the envelope, we will investigate it to find a minimum pulse width by comparing it to the standard form.

$$-2 \ln 2 \left(\frac{\tau}{\tau_0} \right)^2 = \frac{-a\tau^2}{\alpha'^2 \left[\left(\frac{1}{\alpha'} + \frac{1}{\beta'} \right)^2 + a^2 \right]} \quad (\text{A13})$$

$$\tau_0^2 = \frac{2\alpha'^2 \ln 2 \left[\left(\frac{1}{\alpha'} + \frac{1}{\beta'} \right)^2 + a^2 \right]}{a} \quad (\text{A14})$$

Because a is a constant, we can determine the conditions for a minimum by differentiating the numerator with respect to α' . Now, assume that the chirp is a constant and then solve for the dispersion which yields a minimum pulse width.

$$\frac{d}{d\alpha'} \left\{ \alpha'^2 \left[\left(\frac{1}{\alpha'} + \frac{1}{\beta'} \right)^2 + a^2 \right] \right\} = 2\alpha' a^2 + \frac{2}{\beta'} + \frac{2\alpha'}{\beta'^2} = 0 \quad (\text{A15})$$

Solving for the dispersion term, α' , we get

$$\alpha' = \frac{-\beta'}{1 + a^2\beta'^2}. \quad (\text{A16})$$

This is the condition on the dispersion in order to get the minimum pulse width. If we substitute this into (A14) and simplify we get

$$\tau_0^2 = \frac{2 \ln 2}{a + \frac{1}{a\beta'^2}}. \quad (\text{A17})$$

Inserting the expressions for a and β' in the equation above and solving for the input to output pulse width ratio yields

$$\frac{\tau_i}{\tau_o} = \sqrt{1 + \left[\left(\frac{\Gamma_0 \pi^2}{\ln 2} \right) \left(\frac{\tau_i}{T} \right)^2 \right]^2}. \quad (\text{A18})$$

References

1. P. Tournois, “Analogie optique de la compression d’impulsion,” *Compt. Rend. Acad. Sci. (Paris)*, vol. 258, pp. 3839–3842, 1964; and *Ann. de Radioélect.*, vol. 19, pp. 267–280, 1964.
2. S. A. Akhmanov, A. S. Chirkin, K. N. Drabovich, A. I. Kovrigin, and R. V. Khokhlov, and A. P. Sukhorukov, “Nonstationary nonlinear optical effects and ultrashort light pulse formation,” *IEEE J. Quant. Elect.*, vol. QE-4, pp. 598–605, 1968.
3. S. A. Akhmanov, A. P. Sukhorukov, and A. S. Chirkin, “Nonstationary phenomena and space-time analogy in nonlinear optics,” *Sov. Phys.-JETP*, vol. 28, pp. 748–757, 1969.
4. A. Papoulis, *Systems and Transforms with Applications in Optics*, McGraw-Hill, New York, 1968.
5. P. Tournois, J-L Vernet, and G. Bienvenu, “Sur l’analogie optique de certains montages électroniques : formation d’images temporelles de signaux électriques,” *Compt. Rend. Acad. Sci. (Paris)*, vol. 267, pp. 375–378, 1968.
6. B. H. Kolner, “Space-time duality and the theory of temporal imaging,” *IEEE J. Quant. Elect.*, vol. QE-30, pp. 1951–1963, 1994.
7. D. J. Griffiths, *Introduction to Electrodynamics*, Prentice-Hall, Englewood Cliffs, NJ, 1981.
8. A. E. Siegman, *Lasers*, University Science Books, Mill Valley, CA, 1986.
9. J. W. Goodman, *Introduction to Fourier Optics*, McGraw-Hill, New York, 1968.
10. B. H. Kolner, “Generalization of the concepts of focal length and f -number to space and time,” *J. Opt. Soc. Am. A*, vol. 11, no. 12, pp. 3229–3234, 1994.
11. B. H. Kolner, “Active pulse compression using an integrated electro-optic phase modulator,” *Appl. Phys. Lett.*, no. 52, pp. 1122–1124, 1988.
12. I. P. Kaminow and W. M. Sharpless, “Performance of LiTaO₃ and LiNbO₃ light modulators at 4 GHz,” *Appl. Optics*, vol. 6, pp. 351–352, 1967.
13. The loss tangent is used to characterize the loss in a material (heat) due to damping of the vibrating dipole moments. It is defined as $\tan \delta = \sigma/\omega\epsilon_r\epsilon_0$ where σ is the material conductivity, ϵ_0 is the permittivity of space and ϵ_r is

the relative permittivity of the material. Most microwave materials are usually characterized by specifying ϵ_r and $\tan \delta$ at a certain frequency.

14. R. E. Collin, *Field Theory of Guided Waves*, IEEE Press, Piscataway, NJ, 1991.
15. Y. Utsumi, "Variational analysis of ridged waveguide modes," *IEEE Trans. Micro. Theory and Tech.*, vol. MTT-33, no. 2, pp. 111–120, 1985.
16. W. J. Getsinger, "Ridged waveguide field description and application to directional couplers," *IRE Trans. Microwave Theory Tech.*, vol. MTT-10, pp. 41–50, 1962.
17. J. P. Montgomery, "On the complete eigenvalue solution of ridged waveguide," *IEEE Trans. Microwave Theory Tech.*, vol. MTT-19, pp. 547–555, 1971.
18. Purple plague is the common name of a reaction which takes place between pure aluminum and gold when they are in direct contact. With heat and/or time the two metals form distinctive purple compounds that are extremely brittle and destroy the electrical integrity of the plating.
19. F. Gires and P. Tournois, "Interféromètre utilisable pour la compression d'impulsions lumineuses modulées en fréquence," *Compt. Rend. Acad. Sci. (Paris)*, vol. 258, pp. 6112–6115, 1964.
20. E. B. Treacy, "Compression of picosecond light pulses," *Phys. Lett.*, vol. 28A, pp. 34–35, 1968.
21. R. L. Fork, C. H. Brito Cruz, P. C. Becker, and C. V. Shank, "Compression of optical pulses to six femtoseconds by using cubic phase compensation," *Opt. Lett.*, vol. 12, pp. 483–485, 1987.
22. J. R. Klauder, A. C. Price, S. Darlington, and W. J. Albersheim, "The theory and design of chirp radars," *Bell Sys. Tech. J.*, vol. 39, pp. 745–808, 1960.
23. W. J. Tomlinson, R. H. Stolin, and C. V. Shank, "Compression of optical pulses chirped by self-phase modulation in fibers," *J. Opt. Soc. Am. B*, vol. 1, pp. 139–149, 1984.
24. D. Grischkowsky and A. C. Balant, "Optical pulse compression based on enhanced frequency chirping," *Appl. Phys. Lett.*, vol. 41, pp. 1–3, 1982.
25. J. A. Giordmaine, M. A. Duguay, and J. W. Hansen, "Compression of optical pulses," *IEEE J. Quant. Elect.*, vol. QE-4, pp. 252–255, 1968.
26. D. Grischkowsky, "Optical pulse compression," *Appl. Phys. Lett.*, vol. 25, pp. 566–568, 1974.
27. A. A. Godil, B. A. Auld, and D. M. Bloom, "Time-lens producing 1.9 ps optical pulses," *Appl. Phys. Lett.*, vol. 62, pp. 1047–1049, 1993.

28. M. T. Kauffman, A. A. Godil, B. A. Auld, W. C. Banyai, and D. M. Bloom, "Applications of time lens optical systems," *Elect. Lett.*, vol. 29, pp. 268–269, 1993.
29. The author wishes to thank Corey Bennett of Prof. Kolner's group at UCLA Electrical Engineering Department for his essential work on the design of the multiple-pass optical cavity.
30. W. R. Trutna and R. L. Byer, "Multiple-pass Raman gain cell," *Appl. Optics*, vol. 19, pp. 301–312, 1980.
31. T. F. Gallagher, N. H. Tran, and J. P. Watjen, "Principles of a resonant cavity optical modulator," *Appl. Opt. Lett.*, vol. 25, pp. 510–514, 1986.
32. A. E. Siegman, *An Introduction to Lasers and Masers*, McGraw-Hill, New York, 1971.
33. E. P. Ippen, H. A. Haus, and L. Y. Liu, "Additive pulse mode locking," *J. Opt. Soc. Am. B*, vol. 6, pp. 1736–1745, 1989.
34. L. Y. Liu, J. M. Huxley, E. P. Ippen, and H. A. Haus, "Self-starting additive-pulse mode locking of a Nd:YAG laser," *Opt. Lett.*, vol. 15, pp. 553–555, 1990.
35. J. K. Chee, M. N. Kong, E. C. Cheung, and J. M. Liu, "Generation of ultrashort Nd:YLF pulses by cw passive modelocking with a nonlinear external cavity," *Ultrafast Phenomena VII*, vol. 53, pp. 8–10, 1990.
36. P. M. W. French, J. A. R. Williams, and J. R. Taylor, "Femtosecond pulse generation from a titanium-doped sapphire laser using nonlinear external cavity feedback," *Opt. Lett.*, vol. 14, pp. 686–688, 1989.
37. J. Mark, L. Y. Liu, K. L. Hall, H. A. Haus, and E. P. Ippen, "Femtosecond pulse generation in a laser with a nonlinear external resonator," *Opt. Lett.*, vol. 14, pp. 48–50, 1989.
38. F. M. Mitschke and L. F. Mollenauer, "Stabilizing the soliton laser," *IEEE J. Quant. Elect.*, vol. QE-22, pp. 2242–2250, 1986.
39. B. H. Kolner, unpublished, 1994.

